

The dynamical properties of dense filaments in the infrared dark cloud G035.39–00.33^{*}

J. D. Henshaw^{1†}, P. Caselli¹, F. Fontani², I. Jiménez-Serra³, and J. C. Tan⁴

¹*School of Physics and Astronomy, University of Leeds, Leeds LS2 9JT, UK*

³*INAF-Osservatorio Astrofisico di Arcetri, L.go E. Fermi 5, Firenze I-50125, Italy*

²*European Southern Observatory, Karl-Schwarzschild-Str. 2, 85748, Garching, Germany*

⁴*Department of Astronomy, University of Florida, Gainesville, FL 32611, USA*

Accepted 2014 March 5. Received 2014 March 5; in original form 2013 November 16

ABSTRACT

Infrared Dark Clouds (IRDCs) are unique laboratories to study the initial conditions of high-mass star and star cluster formation. We present high-sensitivity and high-angular resolution IRAM PdBI observations of N_2H^+ ($1 - 0$) towards IRDC G035.39-00.33. It is found that G035.39-00.33 is a highly complex environment, consisting of several *mildly* supersonic filaments ($\sigma_{\text{NT}}/c_s \sim 1.5$), separated in velocity by $< 1 \text{ km s}^{-1}$. Where multiple spectral components are evident, moment analysis overestimates the non-thermal contribution to the line-width by a factor ~ 2 . Large-scale velocity gradients evident in previous single-dish maps may be explained by the presence of substructure now evident in the interferometric maps. Whilst *global* velocity gradients are small ($< 0.7 \text{ km s}^{-1} \text{ pc}^{-1}$), there is evidence for dynamic processes on *local* scales ($\sim 1.5\text{--}2.5 \text{ km s}^{-1} \text{ pc}^{-1}$). Systematic trends in velocity gradient are observed towards several continuum peaks. This suggests that the kinematics are influenced by dense (and in some cases, *starless*) cores. These trends are interpreted as either infalling material, with accretion rates $\sim (7 \pm 4) \times 10^{-5} M_\odot \text{ yr}^{-1}$, or expanding shells with momentum $\sim 24 \pm 12 M_\odot \text{ km s}^{-1}$. These observations highlight the importance of high-sensitivity and high-spectral resolution data in disentangling the complex kinematic and physical structure of massive star forming regions.

Key words: stars: formation; ISM: clouds; ISM: individual objects: G035.39-00.33; ISM: kinematics and dynamics; ISM: molecules.

1 INTRODUCTION

Understanding and categorising the initially quiescent phases of massive ($> 8 M_\odot$) star formation is *essential* if we are to develop a complete picture of how massive stars form. Once star formation is under way, the disruptive effect of stellar feedback destroys the primordial information needed to explain their formation. Consequently, the search for massive starless cores (the dense precursors to massive stars), requires the identification of relatively *quiescent* clouds, that have yet to be affected by feedback from massive young stellar objects.

Infrared dark clouds (hereafter, IRDCs), were discovered as extended structures, silhouetted against the bright mid-infrared (MIR) emission observed towards the Galactic centre (Pérault et al. 1996, Egan et al. 1998). IRDCs are categorised as hav-

ing large-masses ($\sim 10^{2-5} M_\odot$; Rathborne et al. 2006, Kainulainen & Tan 2013, hereafter KT13), high-column densities ($N_{\text{H}_2} \sim 10^{22-25} \text{ cm}^{-2}$; Egan et al. 1998, Carey et al. 1998), and low temperatures ($\leq 20 \text{ K}$; Pillai et al. 2006, Peretto et al. 2010, Ragan et al. 2011, Chira et al. 2013), making them ideal environments to study the *initial conditions* of star formation. In addition, the high mass surface densities ($\sim 0.3 \text{ g cm}^{-2}$; Butler & Tan 2012, hereafter BT12) and high volume densities ($\sim 10^{4-6} \text{ cm}^{-3}$; Carey et al. 1998, Rathborne et al. 2006, BT12) of IRDC clumps are most akin to regions of massive star formation (Tan et al. 2013).

This study is the sixth instalment of a series of papers whose goal is to provide a detailed case study of the chemistry, dynamics, and physical structure of a single IRDC, G035.39-00.33. Butler & Tan (2009) (hereafter, BT09) selected 10 IRDCs (due to their high-contrast against the Galactic MIR background) from the sample of 38 IRDCs studied by Rathborne et al. (2006). From this sample, G035.39-00.33, cloud H of BT09, was chosen for further study because: i) it has one of the most extreme filamentary morphologies in the Rathborne et al. (2006) study; ii) it exhibits extended quiescent regions with little or no signatures of star formation activ-

^{*} Based on observations carried out with the IRAM Plateau de Bure Interferometer. IRAM is supported by INSU/CNRS (France), MPG (Germany) and IGN (Spain).

[†] E-mail: phy5jh@leeds.ac.uk

ity (4.5 μm , 8 μm , 24 μm emission; Chambers et al. 2009, Carey et al. 2009); iii) it is relatively nearby, with a kinematic distance of ~ 2900 pc (Simon et al. 2006).

Since 2010, G035.39-00.33 has been revealed to be an extremely complex, globally virialised structure (Paper III; Hernandez et al. 2012), consisting of several, morphologically distinct filaments (Paper IV; Henshaw et al. 2013) exhibiting common velocity gradients (Paper V; Jimenez-Serra et al. 2014), that is in an early stage of evolution (Paper II; Hernandez et al. 2011). Paper I (Jiménez-Serra et al. 2010), discovered the presence of faint and narrow SiO emission ($< 1 \text{ km s}^{-1}$), traced over parsec scales in G035.39-00.33. Two main suggestions were put forward to explain this emission: i) a population of widespread, and undetected low-mass protostars (the IRAM 30 m beam at ~ 87 GHz is $\sim 28''$); ii) the emission may be a large-scale shock product of the cloud formation process. Whilst a population of deeply-embedded protostars cannot be ruled out without higher-angular resolution observations of shocked gas tracers, the second scenario above is supported by two conclusions: i) widespread CO depletion indicates that the IRDC is in an early stage of evolution, and is unaffected by stellar feedback (on global scales; Paper II); ii) in Paper IV, a velocity shift between the dense gas (as traced by N_2H^+) and the highly abundant, lower-density envelope material (as traced by C^{18}O) was observed, that may be indicative of the interaction between filaments. The presence of widespread SiO at the intersection point of filaments, has also recently been identified in G028.23-00.19 (Sanhueza et al. 2013). Paper IV revealed the presence of three filamentary structures of varying density: filament 1, a blue-shifted low-density filament (traced mainly by C^{18}O , with minimal N_2H^+); filament 2, the main IRDC filament; filament 3, a red-shifted component observed in both C^{18}O and N_2H^+ (this density structure was later confirmed in the LVG analysis of Paper V). In addition, these filaments appear to intersect at the location of the most massive core within the mapped region, H6 (mass $\sim 60 M_\odot$ within a radius of 0.15 pc; BT12).

Whilst there is evidence that some IRDCs exhibit multiple velocity components (e.g. G035.39-00.33; Papers IV & V, see also Devine et al. 2011, Sanhueza et al. 2013, Peretto et al. 2013), there are very few studies dedicated to understanding the internal kinematics of their filamentary structures, and how this may relate to star formation. In this paper, a detailed kinematic study of G035.39-00.33 at high-angular resolution ($\sim 4''$) is presented. The focus is the analysis of N_2H^+ ($1-0$); a well-known dense gas tracer, with the $J = 1 \rightarrow 0$ transition having a critical density of $n_{crit} = 1.4 \times 10^5 \text{ cm}^{-3}$ (at 10 K)¹. During the earliest stages of low-mass star formation, N_2H^+ typically traces the cold, dense cores; i.e. the precursors to stars (e.g. Caselli et al. 2002a). In high-mass star-forming regions, however, regions of high-density can extend over parsec scales, resulting in the widespread emission of N_2H^+ (Paper IV). This makes N_2H^+ an ideal diagnostic tool for a detailed study of the kinematic behaviour of the dense filamentary structures in G035.39-00.33. In addition, 3.2 mm continuum emission maps are used for comparison with the N_2H^+ data. Further discussion on the continuum properties is reserved for a later publication (Henshaw et al. 2014, in prep.).

Details of the observations can be found in Section 2. The ob-

servational results are presented in Section 3. The detailed kinematic analysis of these data is presented in Section 4. These results are discussed in Section 5, and in Section 6, the findings are concluded. Finally, example spectra, fit parameters, supplementary position-velocity analysis, and a detailed step-by-step method of our Gaussian fitting routine, and filament classification algorithm can be found in the Appendix.

2 OBSERVATIONS

The N_2H^+ observations were carried out using the Institut de Radioastronomie Millimétrique (IRAM) Plateau de Bure Interferometer (PdBI), France. A 6-field mosaic has been obtained. The final map area is $\sim 40'' \times 150''$ (corresponding to $\sim 0.6 \text{ pc} \times 2.1 \text{ pc}$, at a distance of 2900 pc). The mosaic covers the inner area of the cloud. The PdBI is suited to observing this long but narrow filament as the width of the filament, traced by N_2H^+ ($1-0$), is comparable to the primary beam at ~ 93 GHz ($\sim 54''$). Observations were carried out over six days in May, June and October 2011, in the C and D configurations (using 6 and 5 antennas, respectively) offering baselines between 19 m and 176 m to achieve an angular resolution of $\sim 4''$ at ~ 93 GHz. The narrow-band correlator was configured to cover the N_2H^+ ($1-0$) transition (frequency of the isolated, $F_1, F = 0, 1 \rightarrow 1, 2$, component = 93176.2522 MHz; Pagani et al. 2009), with a spectral window of 20 MHz, which provided a spectral resolution of 0.14 km s^{-1} . In addition, the WideX correlator was used for the 3.2 mm continuum. The line-free channels gave a total bandwidth of ~ 3 GHz. System temperatures varied between 125–150 K. In each observation session, phase and amplitude were calibrated using quasars 1749+096 and 1827+062 (respective fluxes: 5 Jy, and 0.81 Jy). Bandpass calibration was carried out using 1749+096 on all dates except 03/06/2011 and 06/06/2011, in which 3C454.3 (flux = 12.62 Jy) and 3C273 (flux = 11.71 Jy) were used, respectively. Flux calibration was carried out using MWC349 (flux = 1.15 Jy) on all dates. The data reduction was performed using GILDAS²/CLIC as part of the GILDAS software.

In addition to the PdBI data, existing IRAM 30 m N_2H^+ ($1-0$) data has been used to incorporate short-spacings to the interferometric map. The single-dish observations were carried out in August 2008. The large-scale maps were obtained with the On-The-Fly (OTF) mapping mode (for more details on these data see Paper IV). The merging of the two data sets was completed within the GILDAS software package, MAPPING, by using ‘UVSHORT’. The central coordinates of the PdBI data were reprojected such that both data sets have reference coordinates of $\alpha(\text{J2000}) = 18^{\text{h}}57^{\text{m}}08.0^{\text{s}}$, $\delta(\text{J2000}) = 2^\circ 10' 30.0''$. Smoothing the merged PdBI & IRAM 30 m data to the resolution of the 30 m beam at 93 GHz ($\sim 26''$), recovers the 30 m flux to within 10% (see Figure A1).

The merged mosaic was CLEANed using the Hogbom cleaning algorithm (as recommended in cases where sidelobes are prominent) in the GILDAS/MAPPING software. CLEANing was performed using a robust weighting factor of 3.16 (GILDAS task ‘UV_STAT WEIGHT’ provides information on robust weighting parameters). This weighting factor ensures that the sidelobes are reduced sufficiently to remove artefacts from the data, whilst the rms noise is increased by only $\sim 10\%$. Following the CLEAN procedure, the synthesised beam has angular size $3.9'' \times 3.2''$ (position

¹ Calculated using coefficients documented within Schöier et al. (2005) and Daniel et al. (2005), provided by the Leiden Atomic and Molecular Database (LAMDA); <http://home.strw.leidenuniv.nl/~moldata/>

² GILDAS: Grenoble Image and Line Data Analysis System, see <http://www.iram.fr/IRAMFR/GILDAS>

angle = 27°). The data has been converted to units of main beam brightness temperature using the task ‘COMBINE’ in *MAPPING*, by multiplying by 11.35 K (Jy beam⁻¹)⁻¹.

To perform spectral analysis, single spectra have been extracted from individual pixels (0.8'' × 0.8'') within the cube. These data have then been smoothed using a Gaussian weighting (FWHM = the major axis of the synthesised beam ~ 4''). Pixel spacings are equivalent to 0.5 × the major axis of the synthesised beam (~ 2''). The typical spectral RMS noise in each pixel is 0.1 K. The analysis is restricted to the isolated hyperfine component (F₁, F = 0, 1 → 1, 2) of N₂H⁺ (1 – 0) unless otherwise stated. This is because the isolated component is expected to be optically thin (see Section 3.2 for more details).

The 3.2 mm continuum data has also been CLEANed using the Hogbom algorithm. The synthesised beam is 4.2'' × 3.1'', with a position angle of 17.3°. The typical map RMS noise is 0.07 mJy beam⁻¹, estimated from emission free regions. In this work the continuum data is used for comparison only. A full discussion and analysis of the continuum data will be provided in Henshaw et al. (2014; in prep.).

Utilised throughout this paper is the 8 μm extinction-derived, 2'' resolution, mass surface density map of Butler & Tan (2012), as modified by Kainulainen & Tan 2013 (hereafter, KT13) to include corrections for the presence of the near infrared extinction-derived IRDC envelope. When direct comparison with N₂H⁺ data has been made, the mass surface density has been smoothed to an equivalent spatial resolution.

3 RESULTS

3.1 Intensity distribution & moment analysis

Figure 1 displays the results of moment analysis covering the PdBI map. Moment analysis has been performed between 42–48 km s⁻¹ (to incorporate the majority of emission in the average spectrum), and above 0.3 K (the 3σ level). The left-hand panel of Figure 1, compares the spatial distribution of the N₂H⁺ (1 – 0) integrated intensity (black contours; 0th order moment) with the mass surface density, as derived in KT13 (colour scale). To highlight the densest portion of the cloud, the (solid) contours are plotted from 10σ (the dotted contour refers to the 5σ level). The central panel of Figure 1 displays the V_{LSR} map (1st order moment), and is shown here between 44.5–47.0 km s⁻¹ (this narrower velocity range has been chosen to pick out the variation in velocity from the brightest emission). The right-hand panel displays the velocity dispersion of the N₂H⁺ (1 – 0) emission, or 2nd order moment, between 0.0–1.5 km s⁻¹.

It is evident from the left-hand panel of Figure 1, that the N₂H⁺ is extended over a large portion of the cloud. This confirms the result from Paper IV that the dense gas is extended over parsec scales in G035.39-00.33. The emission traces the morphology of the mass surface density very closely. The white cross indicates the position of H6, as determined in BT12 (position: α(J2000) = 18^h57^m08.2^s, δ(J2000) = 2°10'51.7'', corresponding to offset: Δα = 2.99'', Δδ = 21.7''). It is clear from Figure 1 that the peak in N₂H⁺ emission (at offset 1.67'', 22.59'') and the peak of H6, as determined from extinction mapping (BT12), are spatially coincident (within a single PdBI beam).

The velocity (V_{LSR}) distribution map shows that higher velocities are situated towards the Northern and Western regions of G035.39-00.33. There are also localised areas of high-velocity (see

offset 5'', -25''). Since moment analysis is insensitive to multiple spectral features, this may indicate regions where additional velocity components affect the overall trend (see Section 4).

A map of the velocity dispersion is shown in the right-hand panel of Figure 1. The velocity dispersion is fairly constant across G035.39-00.33, with a mean value of 0.45 km s⁻¹, with the exception of a notable increase towards the South-West of H6 (peak value > 1 km s⁻¹). This location coincides with red-shifted velocity peaks evident in the 1st order moment map. In paper IV, a high-velocity component (filament 3; ~ 47 km s⁻¹) was shown to overlap spatially with the “main” IRDC filament (filament 2; 45.63 km s⁻¹) at the location of H6. This may indicate that the velocity dispersion is influenced by the presence of an additional component. The presence of multiple velocity components will be further explored in Section 4. Considering a mean velocity dispersion of 0.45 km s⁻¹, the estimated ratio between the thermal and non-thermal contributions is ~ 7 (for N₂H⁺, with a molecular weight of 29 a.m.u., the thermal contribution to the total dispersion is σ_T = 0.07 km s⁻¹, for gas at 15 K; a reasonable estimate based on the dust temperature within G035.39-00.33; Nguyen Luong et al. 2011). This equates to a Mach number of ~ 2 (c_s = 0.23 km s⁻¹, using a mean mass per molecule of 2.33 a.m.u.), similar to those found in Paper V. The velocity dispersions found are most similar to regions of massive star formation, in which non-thermal motions dominate (e.g. Caselli & Myers 1995).

Figure 2 displays the integrated intensity (colour scale, between 0.0 – 4.0 K km s⁻¹) at the six locations highlighted by the black boxes in the left-hand panel of Figure 1 (these locations have been selected to show a range of spectral features). Overlaid are the individual N₂H⁺ (1 – 0) spectra contained within these regions (isolated component only). A dotted line at 45.8 km s⁻¹ (the mean centroid velocity within the map, as calculated from the moment analysis displayed in the central panel of Figure 1), is highlighted in each spectrum, for reference. The profiles of the N₂H⁺ spectra vary throughout the cloud. In three out of the six regions mapped (regions 2, 3, and 4) there is strong evidence for the presence of multiple velocity components, with further evidence in the remaining regions. Referring back to Figure 1, regions 2, 3, and 4 cover the bulk of the emission around H6. Within the vicinity of H6, sub-structure not evident in the single-dish maps of paper IV is detected (see Section 4).

How the intensity of the emission changes with respect to the velocity of the gas can be seen in the channel maps in Figure 3. This displays the emission (red contours) of N₂H⁺ between 44.0 – 48.0 km s⁻¹ integrated in increments of 0.5 km s⁻¹. In the single-dish maps of paper IV, filaments 2 (45.63 ± 0.03) km s⁻¹ and 3 (46.77 ± 0.06) km s⁻¹, whilst clearly spectrally resolved (due to the high-spectral resolution of the IRAM 30 m backends; ~ 0.07 km s⁻¹), were not resolved spatially (the IRAM 30 m beam at 93 GHz ~ 26''). These velocity components, can now be resolved both spectrally *and* spatially. In the 46.5 km s⁻¹ panel, it is evident that filament 3 follows a different portion of the extinction map compared to the main bulk of material observed at lower velocities.

The bulk of the N₂H⁺ emission exists between 45.0–46.5 km s⁻¹. It appears as though the component identified previously as filament 2 (paper IV; V_{LSR} ~ 45.63 km s⁻¹), can now be subdivided into two structures. This is most evident in panels 45.0 km s⁻¹ and 46.0 km s⁻¹, respectively, with 45.5 km s⁻¹ displaying a transition between the two (this is also evident in the spectra of Figure 2). These components are referred to as F2a and F2b (F2a is the more blue-shifted of the two; see Figure 3).

Although F2a and F2b are similar in their emission peaks,

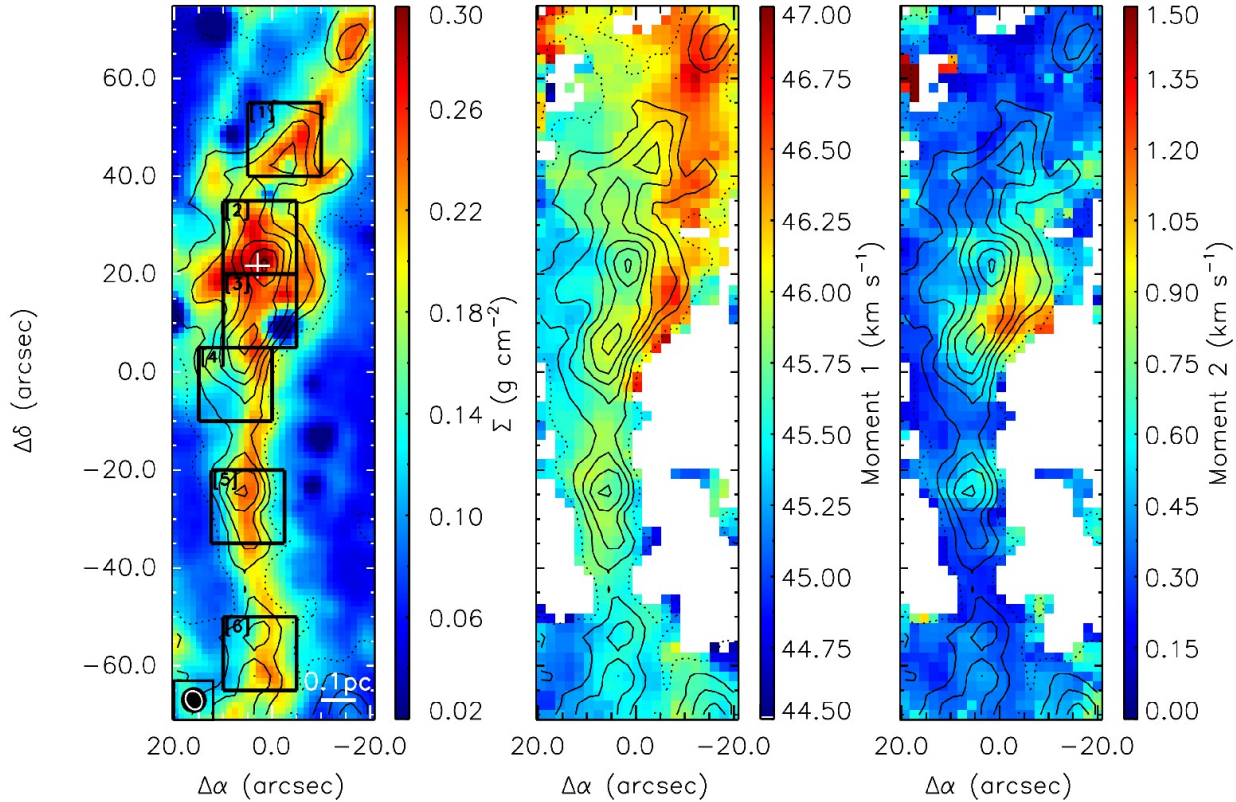


Figure 1. (Left) Integrated intensity contours (black) of N_2H^+ ($1-0$), overlaid on top of the mass surface density plot from Kainulainen & Tan (2013). The spectra have been integrated between 42 km s^{-1} and 48 km s^{-1} , focusing solely on the isolated ($F_1, F = 0, 1 \rightarrow 1, 2$) hyperfine component. Contours increase from 5σ (dotted contour) in steps of 5σ (solid contours; where $\sigma \sim 0.1 \text{ K km s}^{-1}$). The synthesised PdBI beam is shown as a white ellipse in the bottom left-corner (the filled black circle is the effective spatial resolution of the map following Gaussian smoothing). The white cross indicates the position of H6, from Butler & Tan (2012). The boxes indicate the regions of interest that have been selected to show in more detail in Figure 2. (Centre) Map of the velocity field using 1^{st} order moment analysis. (Right) Map of the velocity dispersion using 2^{nd} order moment analysis. The moment analysis has been performed above 3σ , between a velocity range of $42\text{--}48 \text{ km s}^{-1}$. The contours are identical to the left panel.

there are some notable discrepancies. Firstly, F2a is more prominent in the Southern portion of the mapped region, up to H6. F2b, is more prominent in the North. Secondly, not all emission peaks are directly coincident. For instance, the peak observed in the North in F2b (offset $\sim -5'', 50''$; see 46.0 km s^{-1} panel) is not evident in F2a (see 45.0 km s^{-1} panel).

Since F2a is more prominent South of H6, and F2b to the North, treating these two components as a single entity would result in a velocity field that appears to show an abrupt change in velocity at the position of H6. This velocity change at the position of H6 was noted in paper IV (and was also discussed in Paper V, studying various transitions of CO isotopologues), and is indeed observed in the moment analysis here (central panel, Figure 1). If we are to understand the complex kinematics within G035.39-00.33, then the existence of multiple velocity components poses a significant problem that needs to be addressed. Special attention is committed to this topic in Section 4.

3.2 A note on the optical depth of the N_2H^+ ($1-0$) isolated component

This short section is devoted to a discussion on the optical depth of the N_2H^+ ($1-0$) line emission. In paper IV, the hyperfine structure of N_2H^+ ($1-0$) was utilised to show that the isolated component was optically thin (mean *total* optical depth over all 7 hyperfine components < 3 , i.e. an optical depth of the isolated component, ~ 0.33). In addition, the presence of multiple velocity components in N_2H^+ could be verified as the line profiles were similar to the optically thin C^{18}O (the optical depth of C^{18}O was estimated to be $\lesssim 1$ in the densest portion of the mapped region; Paper III).

In this analysis, no optically thin tracer was available. However, the line is assumed to be optically thin for the following reasons: i) this study utilises only the isolated hyperfine component of N_2H^+ ($1-0$), which has a statistical weight of ~ 0.11 (Caselli et al. 1995); ii) if the presence of multiple components was simply an effect attributed to the optical depth, then one would assume that multiple velocity components would be restricted to the high-density regions. However, this is not the case; there is also evidence for multiple velocity components away from H6; iii) multiple peaks are also evident in the N_2H^+ ($3-2$) spectra ($9''$ resolu-

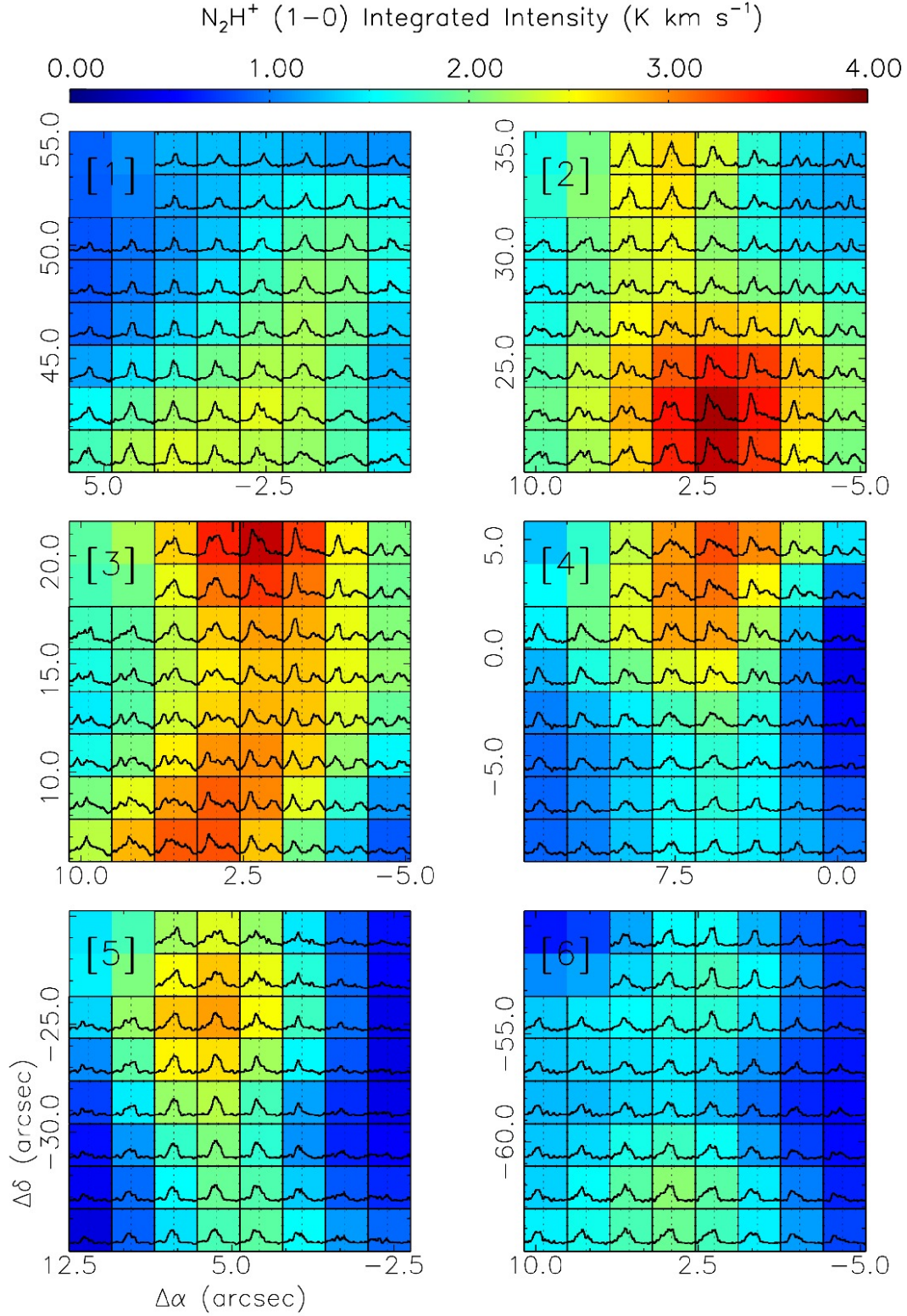


Figure 2. Regions of interest as defined in Figure 1 (left panel). Here the integrated intensity has been overlaid with individual spectra throughout the maps. The intensity has been integrated over the velocity range 42–48 km s^{-1} , and is displayed between 0.0 K km s^{-1} –4.0 K km s^{-1} ($\sigma \sim 0.1 \text{ K km s}^{-1}$). Only the isolated (F_1 , $F = 0, 1 \rightarrow 1, 2$) component is shown, for clarity. The spectra are shown between 44.0–48.0 km s^{-1} (x-axis) and from -0.1–3.5 K (y-axis). The vertical dotted line indicates a velocity of 45.8 km s^{-1} , the mean velocity as calculated from the moment analysis displayed in Figure 1.

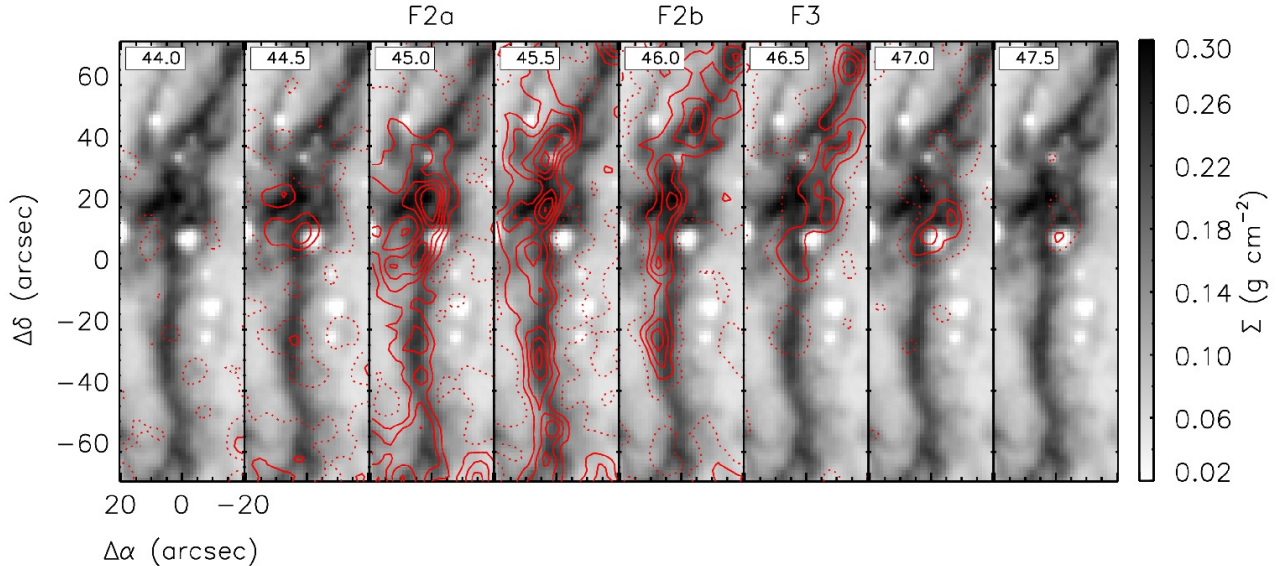


Figure 3. Channel maps of the N_2H^+ ($1-0$) isolated component (F_1 , $F = 0,1 \rightarrow 1,2$). The intensity has been integrated in increments of 0.5 km s^{-1} (velocity in top left corner represents the lower integration limit). Contours are from 0.1 K km s^{-1} (dotted contour; $\sim 5\sigma$ over a 0.5 km s^{-1} velocity range), and increase in 0.2 K km s^{-1} steps (solid contours). Contours are overlaid on the mass surface density plot of KT13. Labels F2a, F2b, and F3 refer to the individual filaments discussed in Section 3.1, and analysed in Section 4.

tion from the IRAM 30 m antenna; see Paper IV), and these peaks align (within uncertainties) with those observed in the PdBI data, when smoothed to an equivalent resolution. The fact that the N_2H^+ ($3-2$) line does not peak in between F2a and F2b (as would be expected if the $J = 1 \rightarrow 0$ transition was optically thick, and the $J = 3 \rightarrow 2$ transition, thin) suggests that they trace similar kinematics, and the $J = 1 \rightarrow 0$ isolated hyperfine component is not significantly affected by optical depth effects; iv) Figure 4 shows the N_2H^+ ($1-0$) integrated intensity versus mass surface density over the whole cloud. Since there is a strong correlation between these two properties (r -value ~ 0.7), and no plateau is observed towards higher extinction (as expected in the case of optical depth effects), this also suggests that the isolated component of N_2H^+ ($1-0$) is optically thin; v) multiple component hyperfine structure fits have been performed (where possible; see Appendix A), and the fit results are consistent with the isolated components being optically thin. Thus, it is likely that F2a and F2b are independent velocity features.

3.3 N_2H^+ column density

The column density of the N_2H^+ ($1-0$) line can be estimated by scaling the integrated intensity of the isolated hyperfine component by its statistical weight (0.11; assuming it is optically thin). The scaled integrated intensity is then used with equation A4 in Caselli et al. (2002b):

$$N_{tot} = \frac{8\pi I_{tot} g_u}{\lambda^3 A g_l J_\nu(T_{ex}) - J_\nu(T_{bg})} \frac{1}{1 - \exp(-h\nu/k_B T_{ex})} \times \frac{Q_{rot}(T_{ex})}{g_l \exp(-El/k_B T_{ex})}, \quad (1)$$

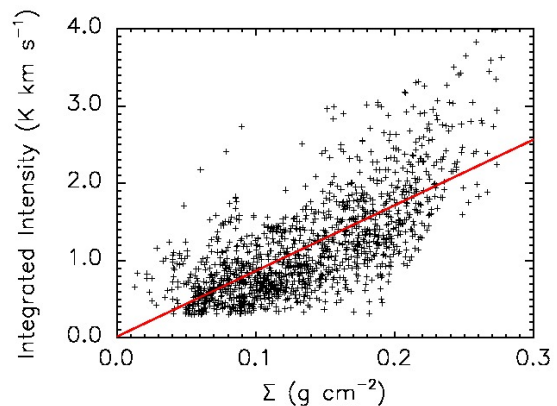


Figure 4. Integrated intensity of N_2H^+ ($1-0$) vs. mass surface density. Intensity has been integrated between $42.0 - 48.0 \text{ km s}^{-1}$. Integrated intensity values are plotted above the typical 3σ uncertainty ($\sim 0.3 \text{ K km s}^{-1}$). The uncertainty in the mass surface density is estimated at $\sim 30\%$ (see KT13 for more details). The red line indicates the best fit to the data.

in this analysis, I_{tot} represents the integrated intensity across *all* of the isolated components (i.e. irrespective of multiple components) scaled by the statistical weight ($I_{tot} = \frac{1}{R_i} \int T_{MB} dv$, whereby R_i is the relative statistical weight ~ 0.11), A is the Einstein coefficient for spontaneous emission ($3.63 \times 10^{-5} \text{ s}^{-1}$; Schöier et al. 2005), g_u and g_l are the statistical weights for the upper and lower states, respectively, $J_\nu(T_{ex})$ and $J_\nu(T_{bg})$ are the equivalent Rayleigh-Jeans excitation and background temperatures. The excitation temperature was estimated from the output parameters of a fit to the hyperfine structure, using GILDAS/CLASS, at the offset of

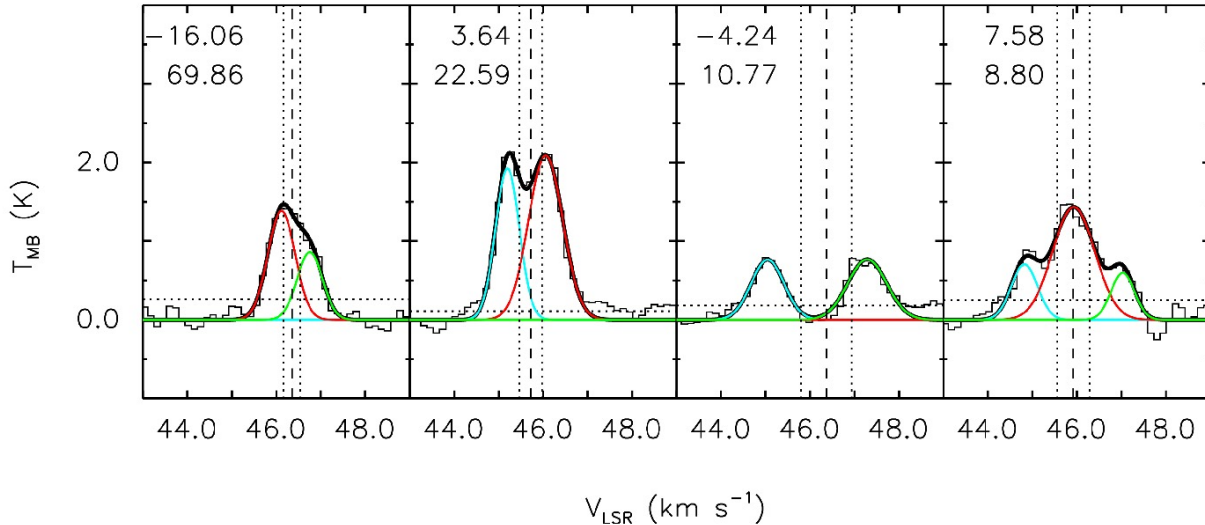


Figure 5. Example spectra from four positions (see top left hand corner of each plot for position: top = $\Delta\alpha$, bottom = $\Delta\delta$ in arc seconds) in the cloud. The vertical dashed line indicates the velocity as calculated from the 1st order moment, whereas the vertical dotted lines refer to the velocity dispersion as calculated from the 2nd order moment (moment analysis performed over a velocity range 42–48 km s⁻¹, and where $T_{\text{MB}} > 0.3$ K). The horizontal dotted line corresponds to the $3\times\text{RMS}$ value for each spectrum. Cyan, red, and green Gaussian profiles are fits to individual velocity components, F2a, F2b, and F3, from the fitting procedure outlined in Appendix D. The black profile indicates the total fit to the line. The fit parameters for each Gaussian component can be found in Table B1.

peak N_2H^+ emission (1.67'', 22.59''), giving a value³ of ~ 7.4 K. $Q_{\text{rot}}(T_{\text{ex}})$ is the partition function, λ and ν are the wavelength and frequency of the $J = 1 \rightarrow 0$ transition, and k_B and h are the Boltzmann and Planck constants, respectively. This equation can therefore be reduced to:

$$N_{\text{tot}}(\text{N}_2\text{H}^+) = 1.3 \times 10^{12} I_{\text{tot}} (\text{K km s}^{-1}) \text{ cm}^{-2}. \quad (2)$$

The column density is estimated for every pixel in the map. The column density at offset (1.67'', 22.59'') is $(4.7 \pm 0.5) \times 10^{13} \text{ cm}^{-2}$. The mean value over the map is estimated to be $(1.3 \pm 0.2) \times 10^{13} \text{ cm}^{-2}$. In the extreme case whereby the optical depth of each of the isolated hyperfine components approach $\tau \sim 1$, a correction factor of ~ 1.6 would need to be made to the column density. However, a case such as this is not observed, and so the correction factor would typically be < 1.6 . In Appendix A an example spectrum is shown (offset = 3.6'', 12.7'', i.e. close to the H6 region), with a multiple-component hyperfine structure fit. In this example, corresponding τ values of the isolated hyperfine components are all < 1 .

As the integrated intensity is directly proportional to the column density (in the optically thin case), the correlation derived in Figure 4 can be used to estimate a fractional abundance of N_2H^+ molecules, with respect to H_2 (as derived from the mass surface density). Assuming a mean mass per molecule of 2.33 a.m.u., the correlation (shown as the red line in Figure 4), implies a constant

fractional abundance of, $[\text{N}_2\text{H}^+/\text{H}_2] = (3.8 \pm 0.1) \times 10^{-10}$, similar to the N_2H^+ abundance found in low-mass dense cores (e.g. Caselli et al. 2002a).

4 ANALYSIS: KINEMATICS OF THE DENSE GAS WITHIN G035.39-00.33

As shown in Section 3, a high-degree of complexity is observed in the N_2H^+ ($1 - 0$) emission towards G035.39-00.33. Fitting these data is challenging for a number of different reasons: i) there are multiple velocity components along the line of sight; ii) the velocity separation between components is $< 1 \text{ km s}^{-1}$ (comparable with the typical FWHM observed; see right-panel of Figure 1); iii) each of these velocity components is likely to exhibit its own velocity structure across the filament, leading to blending of the spectral features. In Paper IV we developed a simple fitting routine (dubbed the Guided Gaussian Fit), that enabled us to separate the molecular line data into individual components. The Gaussian fitting of the PdBI data, however, poses a more significant challenge due to the additional structure observed in the high-angular resolution map.

Analysis of the PdBI data has been performed using a semi-automated Gaussian fitting procedure. Briefly, the technique works by assuming that the profiles of the spectra remain *relatively* constant over suitably small angular distances ($\lesssim 0.1 \text{ pc}$). Therefore, one can reduce the number of spectra to fit by only fitting the average spectrum within a user defined area (see Appendix D for details). The output values from the fit to the average spectrum are then used as free-parameter inputs to each spectrum within the area. By overlapping areas, multiple fits are performed to a single spectrum. This ensures a *smooth* transition between adjacent areas.

³ for details on the estimation of T_{ex} from the HFS output, see the CLASS manual at <http://iram.fr/IRAMFR/GILDAS/doc/html/class-html/>). The fitting procedure also provided an estimate of the optical depth of the line.

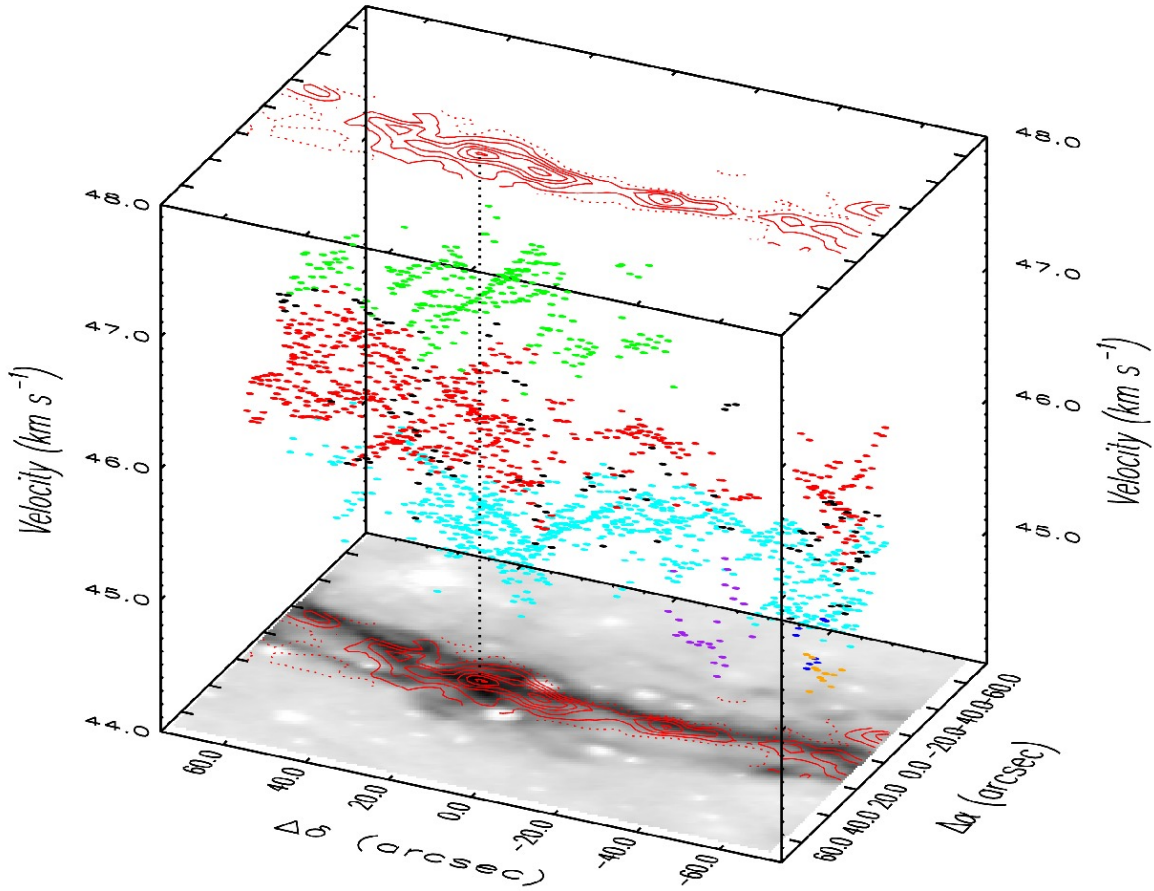


Figure 6. Three dimensional position-position-velocity (PPV) cube showing the centroid velocity of the three velocity components: (cyan) F2a, (red) F2b, and (green) F3, observed across G035.39-00.33. Additional velocity components, C4, C5, and C6, are shown in purple, blue, and orange, respectively (see Appendix D for more details). Unassigned data points are shown in black. The mass surface density map can be seen at the base of the cube, overlaid with N_2H^+ (1 – 0) integrated intensity contours. Contour levels increase from 5σ (dotted contour; where $\sigma \sim 0.1 \text{ K km s}^{-1}$) in steps of 5σ (solid contours), as with Figure 1. The vertical dotted line corresponds to the position of H6.

A minimisation technique is then used to compare fits to individual spectra, selecting the “best fit”. Individual velocity components are then grouped using an algorithm devoted to seeking out similar components within a user defined area. This algorithm follows the same underlying principles as the “Friends In VELOCITY”, FIVE, algorithm developed by Hacar et al. (2013), in that velocity components are grouped based on how closely they are linked in both position and velocity *simultaneously* (by calculating the velocity gradient; see Appendix D), utilising position-position-velocity space.

Figure 5 displays individual spectra towards four positions in our N_2H^+ map (only the isolated hyperfine component is shown). The offset right ascension (top) and offset declination (bottom) are highlighted in the top-left corner of each spectrum. For each spectrum, the Gaussian fit to each velocity component (F2a=cyan; F2b=red; F3=green), and the total fit to the line is overlaid (black). The fit parameters to each Gaussian profile are reported in Table B1. For reference the $3 \times \text{RMS}$ level is highlighted with a horizontal dotted line. These spectra have been highlighted to show the broad range of profiles, and the fitting procedure’s ability to cope

with such diversity. The velocity structure is analysed in more detail in the following sections:

4.1 Centroid velocity

Figure 6 is a position-position-velocity (PPV) representation of the individual velocity components within the cloud. The image shown in position-position space at the base of the figure is the mass surface density map from KT13, overlaid with N_2H^+ contours (identical contours are shown in Figure 1). The vertical dotted line indicates the position of H6, and is used for reference.

Six velocity components are discovered in total. Cyan and red refer to filaments F2a, and F2b, and filament F3 is displayed in green. Velocity components 4, 5, 6 are displayed in purple, dark blue, and orange, respectively. The combined contribution of components 4, 5, and 6 to the overall number of Gaussian fits is $< 5\%$, and they are therefore not considered as “filaments” (percentage contributions of each component can be found in Table D1).

Figure 7 displays a histogram of centroid velocities of F2a,

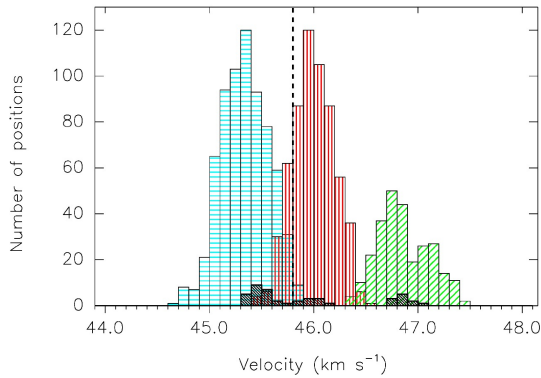


Figure 7. Histogram of the centroid velocity at peak intensity of individual velocity components in both the (colour) PdBI data, and (black) IRAM 30 m data of paper IV, as determined by the Gaussian fitting technique outlined in Appendix D. Filaments 2a, 2b, and 3, are shown in Cyan (horizontal hatch), Red (vertical hatch), and Green (45° hatch), respectively. The vertical dashed line represents the mean velocity derived from the moment analysis in Section 3.1.

F2b, and F3 (red, cyan, and green, respectively), as well as that of the N_2H^+ IRAM30m data (black). In Paper IV the peak at $(46.77 \pm 0.06) \text{ km s}^{-1}$ was interpreted as filament 3. The double peaked component between $\sim 45\text{--}46.5 \text{ km s}^{-1}$ (mean $V_{\text{LSR}} = 45.63 \text{ km s}^{-1}$), was classified as filament 2, the brightest and therefore “main” filament of the IRDC. The dual-peaked velocity of filament 2 was noted in Paper IV and was interpreted as an abrupt change in velocity occurring at the position of H6. Figure 7 shows that F2a and F2b peak at similar velocities to the dual peaks of filament 2 in the single-dish data. This suggests that both components were also spectrally evident in the single dish data. However, the sub-components were not categorised as such as they could not be spatially resolved. There is also a double peak evident in the F3 classification. This can be clearly seen as a peak (in velocity) in Figure 8, in which the V_{LSR} of each velocity component is plotted as a function of offset declination (the possible origins of this structure are discussed in more detail in Section 5.1).

Filaments F2a, F2b, and F3 have mean V_{LSR} values of $(45.34 \pm 0.04) \text{ km s}^{-1}$, $(46.00 \pm 0.05) \text{ km s}^{-1}$, and $(46.86 \pm 0.04) \text{ km s}^{-1}$, respectively. The mean V_{LSR} of F2a and F2b is $(45.67 \pm 0.03) \text{ km s}^{-1}$, which is comparable with the quoted value for filament 2 in paper IV (45.63 km s^{-1}). Velocity separations between individual velocity components are $(0.66 \pm 0.06) \text{ km s}^{-1}$, and $(0.86 \pm 0.06) \text{ km s}^{-1}$, between F2b–F2a, and F3–F2b, respectively. Although components 4, 5, and 6 have similar mean velocities (all $< 45 \text{ km s}^{-1}$), they are separated in position, and there are not enough consecutive data points to conclude that they belong to a single component. In spite of this, it is interesting to note that the velocities of these components are most similar to those derived for filament 1 (Papers IV & V). It is possible that these components may represent compact, high-density portions of filament 1, that are not observed in the low-angular resolution N_2H^+ maps of Paper IV (perhaps due to beam dilution).

The separation between the mean velocities of each individual component are comparable ($< 1 \text{ km s}^{-1}$). Each velocity component has a total 3σ dispersion in V_{LSR} that is roughly equivalent to

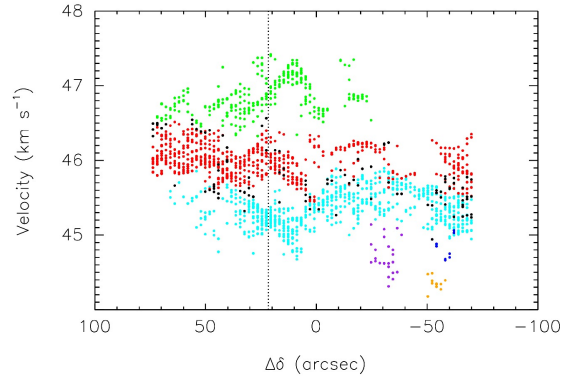


Figure 8. Centroid velocity for filaments F2a (cyan), F2b (red), and F3 (green) as a function of offset declination. Additional velocity components, C4, C5, and C6, are shown in purple, blue, and orange, respectively. Unassigned data points are shown in black. The vertical dotted line refers to the offset declination of H6.

the magnitude of the velocity separation between components. This indicates that there is overlap between velocity components. This can be seen in Figure 6 and even more clearly in Figure 8. Additionally, Figure 8 shows that it is common for unassigned data points (shown in black) to reside at the boundaries of component definitions. These typically represent positions where there is a transition from multiple to single components, i.e. the limit of the fitting method where individual spectral features can no longer be distinguished.

In general, Figures 6 & 8 show that the velocity dispersion over all filaments is broadest slightly South of H6. It is also evident that F2a is more prominent towards the South of H6, while F2b mainly traces the region North of H6 (confirming the result found in Figure 3). F3 is not evident South of $\Delta\delta \sim -30''$, which is consistent with Paper IV. It is noted that there is a gap in the F2b structure at $\Delta\delta \sim -50''$. Whilst the classification scheme identifies the component both above and below $\Delta\delta \sim -50''$ as F2b, further mapping of the Southern region would be needed to establish whether or not this is a truly independent structure (see Appendix D for velocity component classification parameters).

4.2 Velocity gradients

By looking at the V_{LSR} of each individual filament simply as a function of offset declination, as has been plotted in Figure 8, it is clear that each individual velocity component has its own complex structure, exhibiting both global, and local, velocity gradients. It is evident that overall velocity gradients (calculated using a linear fit between the velocity and offset declination) are small in the North–South direction. F2a and F2b have almost negligible *overall* velocity gradients ($0.08 \pm 0.02 \text{ km s}^{-1} \text{ pc}^{-1}$, positive in the North–South direction; and $0.07 \pm 0.01 \text{ km s}^{-1} \text{ pc}^{-1}$, negative in the North–South direction, respectively) between $-70'' \lesssim \Delta\delta \lesssim 70''$. F3 has a positive gradient in the North–South direction, $0.30 \pm 0.04 \text{ km s}^{-1} \text{ pc}^{-1}$ (measured between $-25'' \lesssim \Delta\delta \lesssim 70''$).

Small velocity gradients over the whole cloud indicate that the gas motions are relatively quiescent (in the North–South direction). However, *local* fluctuations along each filament axis, are

large compared to the overall gradient. For instance, between $10'' \lesssim \Delta\delta \lesssim 40''$, F2a and F3 show opposing velocity gradients of magnitude $\sim 1.5 \text{ km s}^{-1} \text{ pc}^{-1}$. In addition, velocity gradients may exist in the East–West direction. Therefore, to analyse the gas motions further, a 2-Dimensional representation of the velocity gradient is required.

The left-hand panel of Figure 9 shows the mass surface density from KT13. Black contours highlight the continuum emission, starting at 3σ (where $\sigma = 7 \times 10^{-2} \text{ mJy beam}^{-1}$) and increasing in steps of 2σ . Overlaid are the extended $4.5 \mu\text{m}$ (green squares; Chambers et al. 2009), $8 \mu\text{m}$ (red open circles), and $24 \mu\text{m}$ emission (red open triangles; Carey et al. 2009), as well as the low-mass cores (yellow squares) and high-mass cores (magenta squares) identified using *Herschel* (Nguyen Luong et al. 2011). The right hand panels show the V_{LSR} maps and spatial location of all three velocity components, as deduced from the Gaussian fitting routine. Overlaid on top of each map are arrows indicating the magnitude and direction of velocity gradients in 2 dimensions. To achieve this we have followed the analysis of Goodman et al. (1993). By assuming the centroid velocities of observed lines take an approximately linear form:

$$V_{\text{LSR}} = V_0 + A\Delta\alpha + B\Delta\delta, \quad (3)$$

whereby $\Delta\alpha$ and $\Delta\delta$ are offsets in right ascension and declination (in radians), least-squares minimisation can be used to estimate values of A and B , using MPFIT2DFUN (Markwardt 2009). The velocity gradient, ∇v , can then be calculated for a cloud at distance D , using (Goodman et al. 1993):

$$\nabla v = \frac{(A^2 + B^2)^{1/2}}{D}, \quad (4)$$

and its direction, $\Theta_{\nabla v}$ (direction of increasing velocity, measured East of North), using:

$$\Theta_{\nabla v} = \tan^{-1}\left(\frac{A}{B}\right). \quad (5)$$

This method has been adapted following the procedure outlined in Caselli et al. (2002a) to calculate multiple gradients within a given region with a good determination of V_{LSR} (seven contiguous positions with significant measurements of V_{LSR}). In the case of the PdBI data, the velocity gradient at the location of a given pixel is estimated only if there are a total of 38 pixels within a circular area of $6''$ (see the black circle in Figure 9). The equivalent pixel area would incorporate at least 7 synthesised beams of the PdBI.

For F2a, the overall velocity gradient (calculated incorporating *all* positions for that filament) has a magnitude of $(0.23 \pm 0.01) \text{ km s}^{-1} \text{ pc}^{-1}$ in a direction $(-168.7 \pm 1.7)^\circ$ East of North. However, the mean magnitude of individual velocity gradients (calculated using the multiple arrow technique) is $(1.83 \pm 0.05) \text{ km s}^{-1} \text{ pc}^{-1}$. The overall gradients for F2b, and F3 have magnitudes, $(0.56 \pm 0.01) \text{ km s}^{-1} \text{ pc}^{-1}$, and $(0.70 \pm 0.02) \text{ km s}^{-1} \text{ pc}^{-1}$, at angles $\Theta_{\nabla v} = (-91.1 \pm 0.2)^\circ$ and $(-132.3 \pm 1.2)^\circ$ East of North, respectively. However, as with F2a, the mean values of individual gradients are significantly larger, with corresponding values of $(1.65 \pm 0.07) \text{ km s}^{-1} \text{ pc}^{-1}$, and $(2.33 \pm 0.11) \text{ km s}^{-1} \text{ pc}^{-1}$, for F2b and F3, respectively. It is concluded therefore, that although overall gradients are observed in each individual filament, the gas motions are dominated by localised flows of material.

In contrast to Paper V, gas motions are highly non-uniform and unique to individual filaments (rather than each filament exhibiting similar North–South velocity gradients). This complexity

is highlighted in F2a. Around H6 (yellow cross) the gas motions flow in multiple directions. East of $\Delta\alpha \sim 10''$, gas motion is directed towards the East. West of here, but North of $\Delta\delta \sim 10''$, a positive South–North gradient is found. The arrows here are pointing towards the continuum core to the North–West of H6. South of $\Delta\delta \sim 10''$, the velocity increases towards the South of H6. The arrows here appear to point in the direction of the two continuum peaks between $-15'' < \Delta\delta < 5''$.

South of H6, between $-70'' \lesssim \Delta\delta \lesssim -15''$, the gas motions are not exclusively directed along the main filament axis. Here, it is evident that the large spreads in velocity observed in Figure 8 are represented by motions perpendicular to the main filament axis. In this area gradients are opposing each other (see position $-20'' < \Delta\delta < -40''$), whereas in the very South ($< -50''$), the velocity gradient is directed from East–West. It should be noted however, that in this Southern location, the velocity does decrease again further to the West, which would, again, indicate opposing gradients (see Figure 9, F2a, between $-10'' < \Delta\alpha < 0''$ and $\Delta\delta < -60''$).

In F2b, around H6, the velocity increases towards the position of the continuum core situated slightly East of the yellow cross. To the North of H6, there is a positive velocity gradient from the North–East of H6, to the North–West corner of the map.

Finally, in F3, the velocity gradient analysis shows a uniform transition from low to high velocity in the North–East to South–West direction just above H6. South of here however, there is evidence for two opposing velocity gradients centred on the continuum peak(s) to the South–West of H6. This peak in continuum is also coincident with $8 \mu\text{m}$ and $24 \mu\text{m}$ emission.

In each filament there is evidence that the velocity gradients are directed towards some of the peaks observed in the continuum emission. This suggests that the continuum peaks are influencing the dynamics of the surrounding gas. We shall return to this in more detail in Section 5.

4.3 Line-width

Figure 10 presents the line-width (defined as the full-width at half-maximum, hereafter FWHM) as derived from the fitting procedure at every position in G035.39-00.33, for filaments F2a (left), F2b (centre), and F3 (right). Black contours highlight the continuum emission (contours are identical to Figure 9).

Figure 10 shows that the distribution of line-widths across each filament is quite varied. Mean line-widths of $(0.83 \pm 0.04) \text{ km s}^{-1}$, $(0.77 \pm 0.04) \text{ km s}^{-1}$, and $(0.71 \pm 0.04) \text{ km s}^{-1}$, are found for filaments F2a, F2b, and F3, respectively.

In general there is no obvious spatial correlation between the continuum and the FWHM. In F2a, broad line-widths of $\Delta v \sim 1.5 \text{ km s}^{-1}$ (equivalent to a Mach number of ~ 2.7 , assuming a gas temperature of 15 K) are observed between $-20'' < \Delta\delta < -30''$. Towards H6, the line-width distribution shows variation with respect to individual continuum peaks ($0.5 \text{ km s}^{-1} \lesssim \Delta v \lesssim 1.5 \text{ km s}^{-1}$).

The left-hand panel of Figure 11 shows a histogram of the ratio between the non-thermal and thermal components of the velocity dispersion, for F2a, F2b, and F3. The non-thermal velocity dispersion is determined from the observed line-width using the

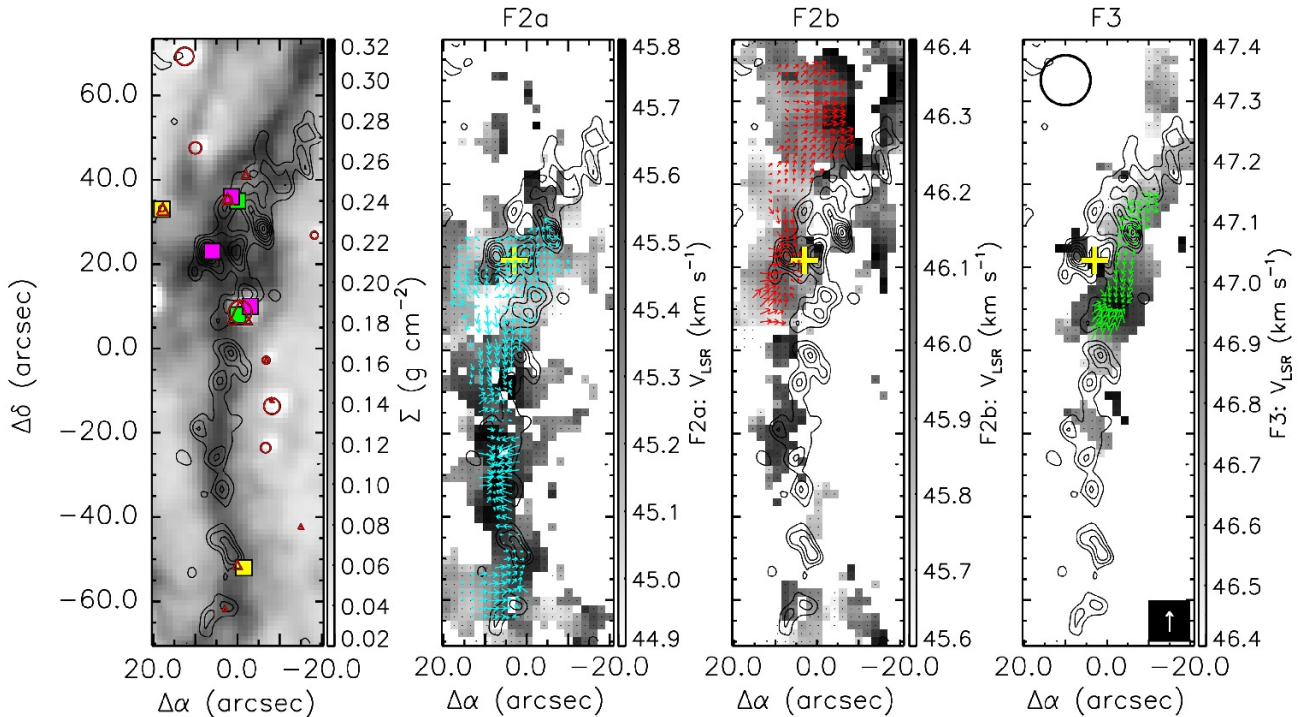


Figure 9. (Left) Mass surface density from KT13, overlaid with the PdBI 3.2 mm continuum (black contours). Continuum contours are from 3σ and increase in steps of 2σ ($\sigma = 7 \times 10^{-2} \text{ mJy beam}^{-1}$, as calculated from emission free regions). Magenta and yellow squares refer to the high-mass and low-mass dense cores identified in Nguyen Luong et al. (2011), respectively. Red circles and red triangles refer to the $8\ \mu\text{m}$, and $24\ \mu\text{m}$ emission, respectively (Carey et al. 2009, Jiménez-Serra et al. 2010), and green squares refer to the “green fuzzies” (extended $4.5\ \mu\text{m}$ emission) identified by Chambers et al. (2009). (Left-centre, right-centre, and right) V_{LSR} maps of filaments F2a, F2b, and F3, as deduced from the Gaussian fitting routine (see text and Appendix D for more details). The velocity ranges are $44.9\text{--}45.8\ \text{km s}^{-1}$, $45.6\text{--}46.4\ \text{km s}^{-1}$, $46.4\text{--}47.4\ \text{km s}^{-1}$, for F2a, F2b, and F3, respectively. Continuum contours are overlaid in black. The yellow cross indicates the position of H6 from BT12. The arrow size depicts the magnitude of the velocity gradient at each position, and each arrow points in the direction of increasing velocity. The white arrow situated in the right panel displays a velocity gradient of magnitude $5\ \text{km s}^{-1} \text{ pc}^{-1}$, and the black circle in the top-left of the panel indicates the spatial extent over which the gradients are calculated (see Section 4.2).

following equation (Myers 1983):

$$(\sigma_{\text{NT}})^2 = (\sigma_{\text{obs}})^2 - (\sigma_{\text{T}})^2 \quad (6)$$

$$\sigma_{\text{NT}} = \sqrt{\frac{\Delta v_{\text{obs}}^2}{8 \ln(2)} - \frac{k_B T_{\text{kin}}}{m_{\text{obs}}}} \quad (7)$$

where σ_{NT} , σ_{obs} , and σ_{T} , refer to the non-thermal, the observed, and the thermal dispersion, respectively. Δv_{obs} refers to the observed line-width (FWHM derived from the fitting procedure), k_B is the Boltzmann constant, T_{kin} is the kinetic temperature of the gas, and finally m_{obs} refers to the mass of the observed molecule (29 a.m.u for N_2H^+). Assuming a gas temperature of 15 K (Pillai et al. 2006, Ragan et al. 2011, Fontani et al. 2012), the thermal dispersion of the gas is $\sim 0.07\ \text{km s}^{-1}$. For F2a, F2b, and F3, mean $\sigma_{\text{NT}}/\sigma_{\text{T}}$ values of 5.4, 5.0, and 4.7 are found, respectively. The right-hand panel of Figure 11 shows a histogram of the ratio between the non-thermal component of the velocity dispersion and the sound speed for a molecule of mean mass 2.33 a.m.u., i.e. the Mach number. The mean Mach numbers derived for filaments F2a, F2b, and F3, are ~ 1.6 , 1.4, and 1.4, respectively. This indicates that the filaments are *mildly* supersonic. It is worth noting that increasing the mean temperature of the cloud to 25 K would

result in the non-thermal motions being comparable to the sound speed. Whilst there are no gas temperature measurements towards G035.39-00.33, the 15 K estimate is based on the dust temperature maps of Nguyen Luong et al. (2011). In these maps, very little temperature fluctuation is observed in the central regions (although these maps are of lower angular-resolution than that studied here). The general trend observed in Figure 11 therefore, is not expected to change significantly.

5 DISCUSSION

5.1 Gas dynamics surrounding continuum peaks

Continuum images (see left-panel of Figure 9) confirm that the region surrounding the H6 location has fragmented into multiple cores (BT12). Between $5'' < \Delta\delta < 40''$, there are 6 continuum peaks in total. Two out of the six cores are associated with observable signatures of star formation, as traced by $4.5\ \mu\text{m}$, $8\ \mu\text{m}$, and $24\ \mu\text{m}$ emission (Chambers et al. 2009, Carey et al. 2009, Jiménez-Serra et al. 2010). In this section the kinematics surrounding both of these continuum cores, plus a further core located to the East of the H6 marker are discussed.

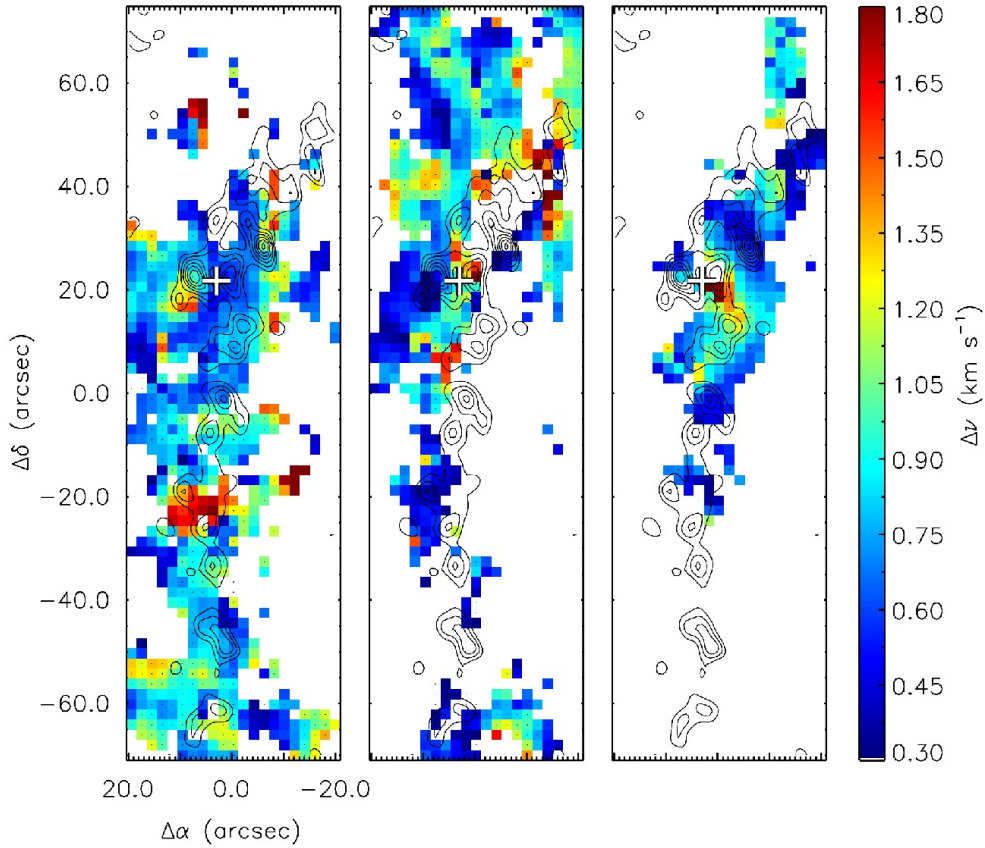


Figure 10. Line-width (Δv , FWHM) maps (colour scale) of filaments F2a (left), F2b (centre), and F3 (right), calculated using the fitting method outlined in Appendix D. Continuum emission is highlighted by the black contours. Contours are the same as in Figure 9. The white cross indicates the position of H6 from BT12.

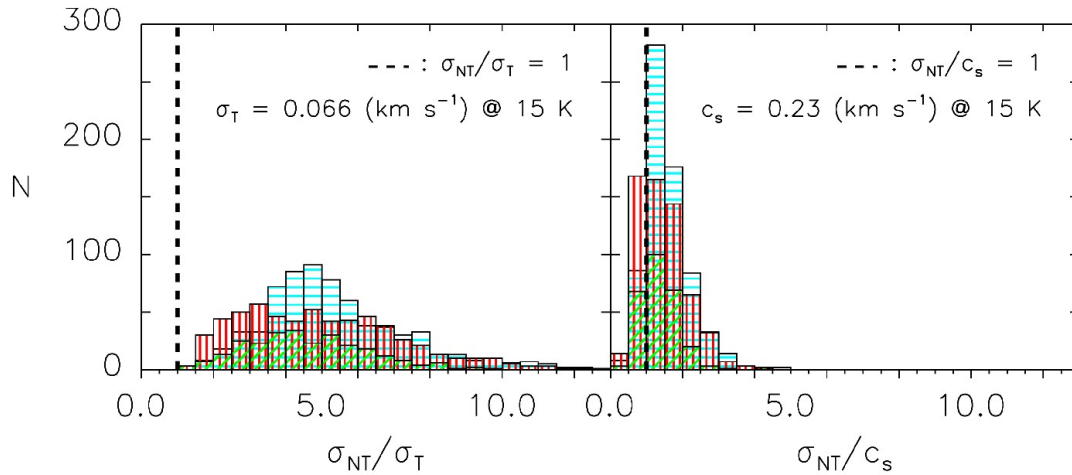


Figure 11. (Left) Histogram of σ_{NT}/σ_T , for filaments F2a, F2b, and F3, shown in cyan (horizontal hatch), red (vertical hatch), and green (45° hatch), respectively. The vertical dashed line refers to $\sigma_{NT}/\sigma_T = 1$. $\sigma_T = 0.066 \text{ km s}^{-1}$, for N_2H^+ (29 a.m.u.) at 15 K. (Right) Histogram of σ_{NT}/c_s (markings have the same meaning as the left-hand panel). The sound speed, c_s is estimated for a mean molecular mass of 2.33 a.m.u. and has a value $\sim 0.23 \text{ km s}^{-1}$.

The continuum peaks discussed in this section have been labelled N, E, and SW, in the top panel of Figure 12. Overlaid are the velocity gradients, closest to the E and SW cores, observed in F2b and F3. The light coloured arrows are identical to those in Figure 9, whereas the darker arrows represent the velocity gradients calculated from the V_{LSR} of 27 pixels (i.e. the constraint imposed in Section 4.2 has been relaxed). This gives us a better idea of the spatial extent of the velocity gradients, but they are not included in any analysis due to their lower significance (see Section 4.2 for further description of the velocity gradient analysis). It is stressed that, *the arrows in the velocity gradient analysis do not indicate the direction of flow of gas, they simply point towards the direction of increasing velocity*. Therefore, depending on the orientation, and physical structure of the cloud, there could be several explanations for the observed velocity structure. In this discussion two *opposing* scenarios are considered that may explain the observed pattern of velocity gradients: i) infalling material, or ii) outflowing material.

5.1.1 Scenario 1: Infall

Due to the symmetry in the arrow pattern towards the SW core, we focus on this continuum peak for further discussion. In the infall scenario, the arrows would depict a flow of N_2H^+ converging onto the SW continuum core. The mean magnitude of the velocity gradients towards the SW core is $\sim 2.5 \text{ km s}^{-1} \text{ pc}^{-1}$ over a spatial extent of $\sim 0.5 \text{ pc}$. This mean velocity gradient is comparable with those observed within the Serpens South cluster-forming region ($1.4 \text{ km s}^{-1} \text{ pc}^{-1}$ measured over $\sim 0.33 \text{ pc}$; Kirk et al. 2013) and the DR21 filament ($0.8\text{--}2.3 \text{ km s}^{-1} \text{ pc}^{-1}$ measured over $\sim 80''$, equivalent to $\sim 0.7 \text{ pc}$ using the distance of the DR21 ridge as 1700 pc ; Schneider et al. 2010). Kirk et al. (2013) and Friesen et al. (2013) interpret velocity gradients in Serpens as flow of material towards star forming regions within the filament. This interpretation arises from the assumption that the filamentary structure is inclined along the line of sight, with respect to the observer. In the case of the Serpens, inclining the cloud towards the observer results in accretion flows towards the Serpens South Cluster (Kirk et al. 2013).

In the case of G035.39-00.33, if the velocity gradient is depicting flow of material onto the SW core, then the geometry must be different from that observed in Serpens. This is because rather than a single North–South velocity gradient, there are two opposing velocity gradients. The velocities either side of the SW core increase towards a maximum. Geometrically, this *may* be explained by an arced filament.

This geometry is further explored in the bottom left-hand panel of Figure 12. For simplicity, rather than an arc, the filament is assumed to be a “kinked” cylinder, with angles Θ and Φ representing the inclination of each end of the cylinder with respect to the plane of the sky. Adopting the same reference system as Kirk et al. 2013, 0° is parallel to the plane of the sky, whereas 90° lies directly along the line of sight. $v_{\text{acc,sky}}$ and $v_{\text{acc,los}}$ represent the velocity of the accreting material in both the plane of the sky, and that along the line of sight, respectively. In the reference frame of the SW continuum peak, the filament gas (to the North and South of the core) is blue-shifted relative to the core (see grey-scale of F3 panel of Figure 9). If the filament was structured as shown in the bottom-left panel of Figure 12, then this would imply gas accretion *along* filaments towards the core. In the context of the main IRDC filament ($v_{\text{mean}} = 45.8 \text{ km s}^{-1}$, as calculated from the moment analysis of Section 3.1), F3 as a whole is red-shifted. v_{fil} represents the velocity of the F3 system (core + filament), and this is assumed to be equivalent to the velocity at the location of the continuum peak

($\sim 47.4 \text{ km s}^{-1}$). If $v_{\text{acc,los}} < (v_{\text{fil}} - v_{\text{mean}})$, a global red-shift of F3 will be observed with respect to v_{mean} .

The mass flow along the filament is estimated by first obtaining an approximate value for the mass contained within the dotted area surrounding the SW core in the top panel of Figure 12. The total mass surface density (taken from KT13) contained within this region is converted to a mass of $\sim 96 M_\odot$. The mass surface density of the filament envelope is estimated by calculating an average value (per pixel) from several polygons, selected to be below a mass surface density of 0.07 g cm^{-2} (i.e. $10 \times$ the lower limit probed by the near infrared extinction map; see KT13 for discussion). Subtracting the estimate for the envelope contribution ($\sim 21 M_\odot$), gives a total filament mass of $75 M_\odot$.

This mass estimate incorporates *all* filaments within the dashed area. To estimate the contribution of F3 to the total mass, it is assumed that all filaments have the same (constant) fractional abundance of N_2H^+ . By using the intensities and line-widths derived from the Gaussian fitting routine, one can calculate the relative contribution each filament makes to the total mass in the specified area. The percentage contribution F3 makes to the total integrated intensity (and therefore mass) in the area is $\sim 46\%$. The mass contribution of F3 is therefore $(34.5 \pm 17) M_\odot$ (estimating a $\sim 50\%$ uncertainty in the mass due to 30% and 20% uncertainties in the mass surface density and distance, respectively). This gives a mass per unit length, $M/L_{\text{obs}} = m = (69 \pm 37) M_\odot \text{ pc}^{-1}$, whereby L_{obs} is the observed filament length of $\sim (0.5 \pm 0.1) \text{ pc}$ (i.e. the length of the dotted box in Figure 12).

The mean line-width (Δv_{obs}) of F3 in this region is 0.61 km s^{-1} . The total 1-D velocity dispersion (of the mean molecule) is calculated using (Fuller & Myers 1992):

$$\sigma_{\text{TOT}} = \sqrt{\frac{\Delta v_{\text{obs}}^2}{8 \ln(2)} + k_B T_{\text{kin}} \left(\frac{1}{\mu m_H} - \frac{1}{m_{\text{obs}}} \right)} \quad (8)$$

whereby μ is the atomic weight of the mean molecule (2.33), and m_H is the mass of a Hydrogen atom. The above line-width therefore, corresponds to a 1-D velocity dispersion of $\sigma_{\text{TOT}} \sim (0.340 \pm 0.03) \text{ km s}^{-1}$ (this uncertainty incorporates both the error in the measured FWHM (given the Gaussian fitting routine) $\sim 7\%$, and an estimated 33% uncertainty on the temperature, i.e. $15 \pm 5 \text{ K}$). The equation for the virial mass per unit length for an isothermal self-gravitating cylinder (Stodólkiewicz 1963, Ostriker 1964) as modified to include the total velocity dispersion of a mean molecule (i.e. including both the thermal and non-thermal contribution to support; Fiege & Pudritz 2000) is:

$$(M/L)_{\text{crit}} = m_{\text{crit}} = \frac{2\sigma_{\text{TOT}}^2}{G}. \quad (9)$$

This gives a value of $m_{\text{crit}} = (53 \pm 9) M_\odot \text{ pc}^{-1}$, i.e. $m/m_{\text{crit}} = 1.3 \pm 0.7$. This value is similar to that derived by Busquet et al. (2013) for several filaments in the G14.225–0.506 complex.

The velocity gradients directed towards the continuum peak are not symmetric (North of the central position, and South of this point have mean gradients of $\sim 2 \text{ km s}^{-1} \text{ pc}^{-1}$, and $3 \text{ km s}^{-1} \text{ pc}^{-1}$, respectively). It is noted however, that this may simply be a geometric effect caused by the kink in the filament. For simplicity, the velocity gradient at each point is assumed to be constant. Assuming that the Northern portion of the filament is inclined at $\Theta = 45^\circ$ (this is an arbitrary choice), would result in the Southern portion being inclined by $\Phi = 55.6^\circ$ (or $\Theta = 124.4^\circ$). The flow of mass along the filament, \dot{M} , is calculated using (Kirk et al.

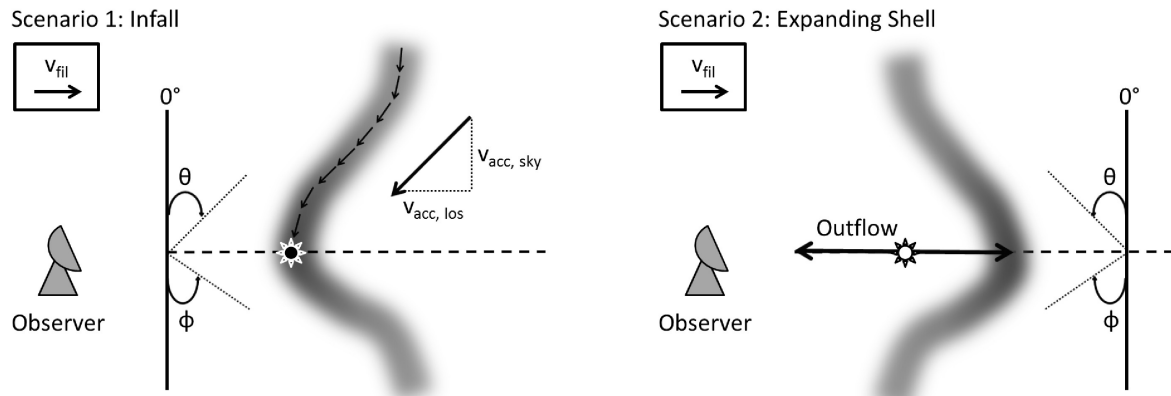
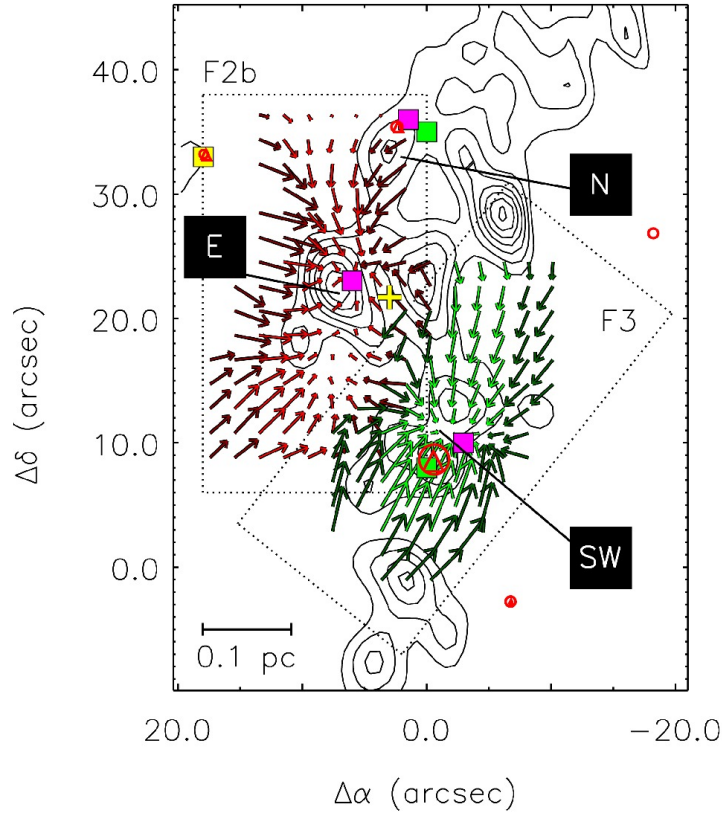


Figure 12. (Top) A close up image of the region surrounding H6. The size and direction of the arrows correspond to the magnitude and direction of the velocity gradient (pointing in the direction of increasing velocity). Dark green and dark red arrows refer to the velocity gradient calculated at each point, using velocities from the surrounding 27 pixels (note - this is used for a spatial representation only, and not used in the analysis), light green and light red arrows refer to the velocity gradient calculated from the surrounding 38 pixels, for F2b and F3, respectively (see Section 4.2 for details). The symbols have the same meaning as in the left panel of Figure 9. (Bottom) Schematics to explain the velocity gradient pattern observed in the top panel. In both cases, v_{fil} is the global redshift of F3, Θ is the inclination of the Northern part of the filament with respect to the plane of the sky, and Φ is the inclination of the Southern part of the filament with respect to the plane of the sky (increasing from the South). In the case shown, $\Theta = 45^\circ$, and $\Phi = 55.6^\circ$ (these have been arbitrarily chosen, although the difference in angles is used to explain the difference in the magnitude in the observed velocity gradient). The left panel describes Scenario 1 (see Section 5.1.1), in which the observed velocity pattern would suggest that material is infalling towards the continuum peak situated at the apex of the filament. The right panel describes Scenario 2 (see Section 5.1.2), in which the protostar is in fact situated at a lower velocity (with respect to the apex), and the observed velocity pattern may be explained by the interaction of an outflow from the forming protostar with the surrounding dense gas (only F3 is shown).

2013):

$$\dot{M} = v_{acc}m, \quad (10)$$

where v_{acc} is the velocity of the accreting material, and m is the mass per unit length. Accounting for projection effects, Equation 10 can be rewritten:

$$\dot{M} = \frac{\nabla v M}{\tan(\Theta)}, \quad (11)$$

using $v_{acc,obs} = \nabla v L_{obs}$, where $v_{acc,obs}$ and L_{obs} are the *observed* line of sight accretion velocity (attributed to the velocity change along the filament), and the observed filament length, respectively (these values are subject to inclination effects). Here, ∇v is the calculated velocity gradient. Assuming an inclination angle of 45° North of the core, corresponding to 55.6° to the South (see Figure 12, bottom left-hand panel), and a velocity gradient, $\nabla v_{acc,los} = (2.0 \pm 0.1) \text{ km s}^{-1} \text{ pc}^{-1}$ (the mean value calculated North of the core), a total mass accretion rate of $\sim (7 \pm 4) \times 10^{-5} M_\odot \text{ yr}^{-1}$ is found. Figure 13 shows how the mass accretion rate would vary with inclination angle.

A value for the free-fall time of the cylinder, assuming homologous collapse, is estimated following the analysis of Pon et al. (2012):

$$\tau_{1D} = \tau_{3D} A \sqrt{\left(\frac{2}{3}\right)}, \quad (12)$$

where τ_{1D} is the cylinder collapse timescale, for a cylinder of aspect ratio, A , and where τ_{3D} is the classical free-fall timescale for the collapse of a sphere with an equivalent (constant) volume density ($\tau_{3D} = \sqrt{(3\pi)/(32G\rho)}$). At a filamentary mass flow rate of $7 \times 10^{-5} M_\odot \text{ yr}^{-1}$, $\sim (36 \pm 25) M_\odot$ will be accumulated at the central continuum core within an estimated free-fall time of $(5 \pm 3) \times 10^5$ yrs (for a cylinder of aspect ratio, $A = L_{obs}/2r \sim 2.8 \pm 0.8$, and $\tau_{3D} \sim (2.3 \pm 0.9) \times 10^5$ yrs), i.e. similar to the mass of the filament within this region.

A filamentary mass flow of $7 \times 10^{-5} M_\odot \text{ yr}^{-1}$ is approximately twice that observed towards the Serpens South cluster ($3 \times 10^{-5} M_\odot \text{ yr}^{-1}$; Kirk et al. 2013). It is also greater than that traced towards *specific continuum peaks* in the Serpens South cluster-forming region ($1.4 \times 10^{-5} M_\odot \text{ yr}^{-1}$; Friesen et al. 2013). In SDC13, Peretto et al. (2014) estimate a mass accretion rate of $2.5 \times 10^{-5} M_\odot \text{ yr}^{-1}$ towards the convergence point of three filamentary structures, whose velocity patterns evoke a similar structure to that discussed in Figure 12. Towards SDC335.579-0.272 Peretto et al. (2013) quote a global mass infall rate of $2.5 \times 10^{-3} M_\odot \text{ yr}^{-1}$. However, the *filamentary* mass accretion rate ($7 \times 10^{-4} M_\odot \text{ yr}^{-1}$; a factor of 10 larger than that observed in the F3 filament), is attributed to 6 filaments. In addition, the mass flow rate within F3 is much smaller than that calculated in Paper V ($5 \times 10^{-3} M_\odot \text{ yr}^{-1}$), estimated from the velocity gradients observed in CO emission using the IRAM 30 m telescope. This will be discussed further in Section 5.2.

This velocity pattern is not isolated to this core. Velocity gradients of F2b point towards the ‘E’ continuum peak (see Figure 12). Using the same geometry outlined above for this continuum peak, a similar mass accretion rate of $\sim (8 \pm 4) \times 10^{-5} M_\odot \text{ yr}^{-1}$ is estimated. The mass per unit length of F2b in this region is $(115 \pm 56) M_\odot \text{ pc}^{-1}$; greater than the critical mass per unit length, $m_{crit} = (59 \pm 11) M_\odot \text{ pc}^{-1}$, by a factor of $\sim 2 \pm 1$. The free-fall time estimated for this region is $(2 \pm 1) \times 10^5$ yrs (where $L_{obs} = 0.45 \text{ pc}$, and $r = 0.13 \text{ pc}$). Therefore, within a single free-fall

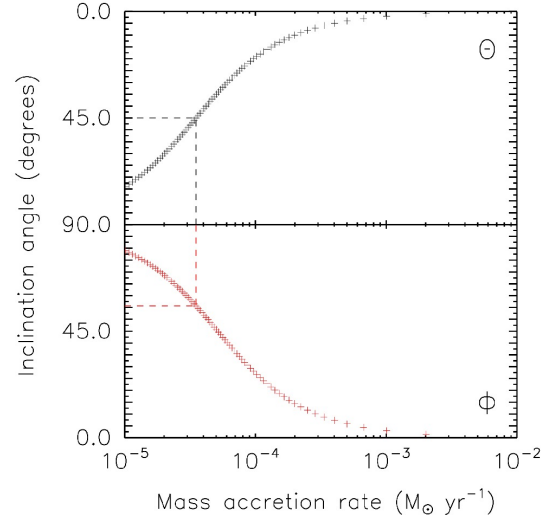


Figure 13. Filamentary mass flow rate versus inclination angle for the velocity gradient pattern surrounding the SW core. Highlighted by dashed lines are the mass accretion rates for the Northern (black) and Southern (red) portions of the filament inclined at angles, $\Theta = 45^\circ$ and $\Phi = 55.6^\circ$ (see bottom left-hand panel of Figure 12). The summation of the two dashed accretion rates gives the total mass accretion rate along filament F3, $\dot{M} \sim 7 \times 10^{-5} M_\odot \text{ yr}^{-1}$.

time, assuming a constant accretion rate, the core will accrete an additional $\sim (16 \pm 11) M_\odot$ of material.

Similar geometry to that illustrated in Figure 12 has been previously used to explain filamentary accretion by Balsara et al. (2001). Here material is directed along filamentary structures, decelerating towards a core situated at the apex of two cylindrical filaments. In these observations, the magnitude of the velocity gradient decreases towards the central region. However, this alone is *not* an indication that the mass flow is decelerating towards the centre of the continuum peak. The reduction in velocity gradient towards the centre is because each gradient is calculated from a relatively large area (see Section 4.2). Therefore, towards the centre of the core, the area over which the calculation is performed incorporates velocities that oppose each other (see top-left of F3 panel in Figure 9). However, it is possible to estimate how the V_{LSR} of the surrounding material changes with respect to the peak velocity using:

$$\nabla v_i = (V_{LSR,peak} - V_{LSR,i})/d, \quad (13)$$

whereby $V_{LSR,peak}$ is the maximum value of velocity (offset = $-2.27'', 10.77''$), $V_{LSR,i}$ is the velocity of a surrounding point, and d is the angular separation between those points. The velocity gradients both to the North, and South of the continuum peak decrease with decreasing angular separation, i.e. $\nabla v_n (\text{km s}^{-1} \text{ pc}^{-1}) = (1.5 \pm 0.1) * d + (2.5 \pm 0.1)$, and $\nabla v_s (\text{km s}^{-1} \text{ pc}^{-1}) = (27.2 \pm 0.1) * d + (0.8 \pm 0.1)$, respectively. This implies that the velocity gradient is largest at both ends of the filament, as predicted during homologous free-fall collapse of cylinders (e.g. Myers 2005, Peretto et al. 2007, Pon et al. 2011). However, it is noted that this decreasing gradient (with respect to the core) may simply be a geometric effect. If the filament has an arc-like structure, a constant accretion velocity may appear as a deceleration towards the core (along the line of sight) as velocity is ‘‘lost’’ to the plane of the sky.

High-angular resolution observations of infall tracers may

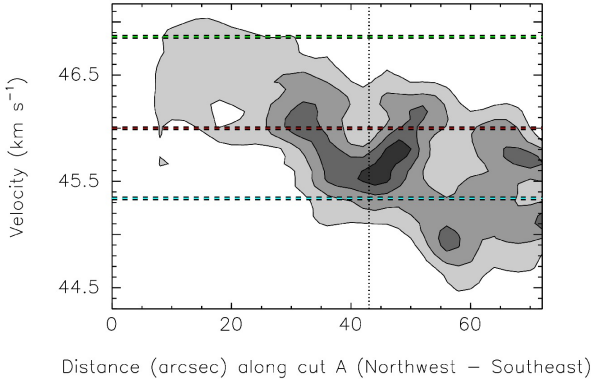


Figure 14. Position-Velocity diagram of cut A (see red dot-dashed line in Figure C1). The filled contours are in units of main beam brightness temperature, and correspond to the 5σ , 10σ , 15σ , and 20σ levels (where $\sigma \sim 0.1$ K). The vertical dotted line refers to the location of continuum peak N (see top panel of Figure 12). Horizontal dashed lines refer to the mean V_{LSR} of each of the three filaments F2a, F2b, and F3 (seen in cyan, red, and green, respectively).

help to constrain some of the questions this geometry raises (c.f. the analysis of Kirk et al. 2013 exploiting HNC self-absorption to estimate infall rates).

5.1.2 Scenario 2: Expanding shell

An alternative scenario would involve the opposite geometry to that discussed above. In this case, the N_2H^+ emission, and the velocity pattern observed may be explained by an expanding shell of dense gas, possibly due to the presence of outflows, and/or stellar winds (see bottom right-hand panel of Figure 12 for a schematic). In symmetry with the infall scenario, only the gas associated with F3 is depicted. The SW peak is coincident with $8 \mu\text{m}$, and $24 \mu\text{m}$ emission, and there is tentative evidence for a high-velocity, red-shifted wing, observed in CO (1-0) at this location (suggestive of outflowing material; Figure A3, for the CO spectrum at this location), which would support this scenario.

Additional supporting evidence for this scenario arises from the velocity structure of core labelled ‘N’ in Figure 12. Figure 14 is a position-velocity (hereafter, PV) slice taken through core N (for further discussion on the PV analysis including the location of the PV slices see Figure C1 and Appendix C). There is an interesting ‘U’-shaped structure (above 10σ) evident between $25'' \lesssim D \lesssim 50''$ (where ‘D’ corresponds to the distance along the PV slice), centred on $\sim 40''$ (Figure 14). This corresponds to the offset location of core N. Such structures have been discussed by Arce et al. (2011), who have modelled expanding bubbles in a turbulent medium and applied this to shell-like structures in Perseus. If the source is located in the centre of the filament, a ring-like structure will be observed in the PV plane. However, Arce et al. (2011) show that if the source is located to the near, or far side of the natal filament/cloud, then emission (of the filament/cloud) in the PV plane would be in a U-shape, either red-shifted or blue-shifted away or towards the observer, respectively. Relating this back to core N, the observed emission pattern in the PV analysis may indicate the interaction between an embedded protostar and the surrounding dense gas (and this may therefore be analogous to the SW core).

Similar structures are also observed towards the SW core (see

‘C’-shaped structures in slices B4–B6 in Figure C4, which dissect the SW core). However, such patterns may simply be explained due to the emergence of additional components (also note that F3 is detected away from the SW core; c.f. slices A0–A4 in Figure C3). This is therefore inconclusive. It is noted however, that the velocity gradient arrows of F2a show a similar pattern to those seen in F3, but in the opposite direction, i.e. arrows point away from the SW core (see Figure 9). The fact that the apex of both the F2a and F3 structures are not directly coincident (there is a positional separation of the apex of 0.17 pc), could be explained by an asymmetric expansion of the shell.

The expanding shell scenario would suggest that the SW continuum core is situated at an intermediate velocity between F2a and F3 (i.e. at a velocity most similar to F2b $\sim 46 \text{ km s}^{-1}$). One can crudely estimate the momentum of the swept up material using:

$$P_{\text{shell}} = M_{\text{shell}}(V_{\text{LSR,peak}} - V_{\text{LSR,edge}}), \quad (14)$$

whereby M_{shell} is the mass of the shell (i.e. of filament F3) estimated in the previous section ($34.5 \pm 17 M_{\odot}$), $V_{\text{LSR,peak}}$ is the peak velocity in the system, and $V_{\text{LSR,edge}}$ is the velocity at the boundary of the velocity gradient analysis. The velocity difference ($V_{\text{LSR,peak}} - V_{\text{LSR,edge}}$) is $\sim 0.7 \text{ km s}^{-1}$, which gives a momentum of $\sim 24 \pm 12 M_{\odot} \text{ km s}^{-1}$. This momentum is smaller than those observed towards expanding shells in Perseus (typical values $> 100 M_{\odot} \text{ km s}^{-1}$, although it is dependent on the mode of star formation; Arce et al. 2011). In addition, the observed spatial extent of the Perseus shells are larger (~ 1 pc, compared with 0.2 – 0.3 pc in G035.39-00.33). However, Quillen et al. (2005) report smaller cavities (of the order 0.1 – 0.2 pc), with velocity widths ~ 1 – 3 km s^{-1} in NGC 1333, comparable to the peak velocity difference between F2a and F3 (see Figure 8). In this scenario, “filaments” or, more correctly, shells in G035.39-00.33 may have originally made up a single structure that has subsequently been separated as a natural consequence of the dynamic process of star formation.

It must be noted however, that whilst there is *some* evidence for broad red-shifted emission of CO (1-0) at the SW core, no blue-shifted emission is evident at the location of the F2a apex. In addition, in the region of the SW core, filaments F2a and F3 provide contributions of 49% and 46%, to the total integrated intensity (the remaining 5% is attributed to F2b), respectively. This would suggest therefore, that if the continuum peak was situated at an intermediate velocity, this position is almost devoid of N_2H^+ emission, as it has been “swept up” by the expanding shell. However, N_2H^+ emission is typically detected in the regions surrounding forming protostars (e.g. Fontani et al. 2008, Tobin et al. 2013), rendering this unlikely. Finally, as evidenced in Figure 10, no obvious broadening of the lines is observed towards the apex of these structures. If F2a and F3 are treated as a single (expanding shell) entity, as in the moment analysis of Figure 1, a broadening of the dispersion is observed. However, as can be clearly seen from offset location ($-4.24''$, $10.77''$) in Figure 5, there are two *Gaussian* components, that show no evidence of line-wings. Follow-up high-angular resolution observations of molecular outflow, and shocked gas tracers are needed in order to validate this scenario.

5.2 Disentangling the complex kinematics of G035.39-00.33

The “simple” picture of G035.39-00.33 appearing as a single filamentary structure in the extinction map of KT13, is a deceptive one. Previous single-dish studies (Papers I, IV, & V) have revealed that G035.39-00.33 is in fact comprised of multiple filamentary

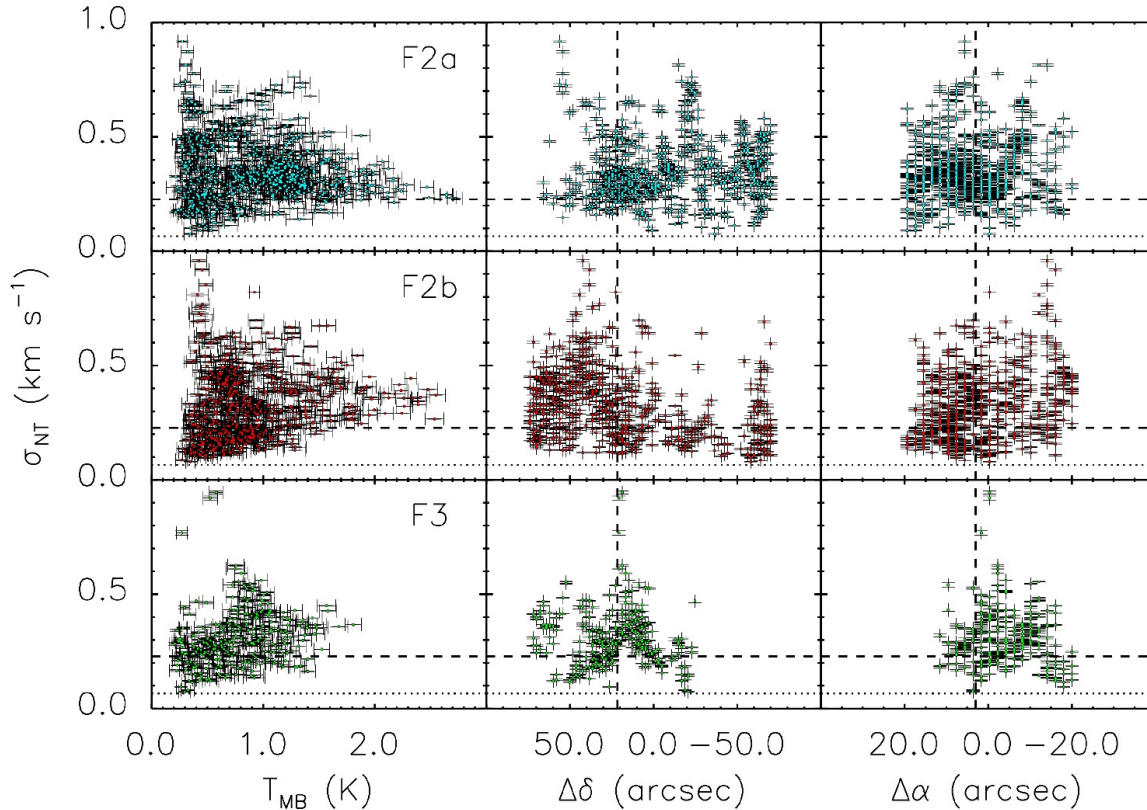


Figure 16. Non-thermal velocity dispersion (σ_{NT}) for F2a, F2b, and F3, derived from N_2H^+ FWHM for every position in the cloud, versus (from left-to-right) main beam brightness temperature (T_{MB}), offset declination ($\Delta\delta$), and offset right ascension ($\Delta\alpha$), respectively. In each plot, the horizontal dotted and horizontal dashed lines refer to the approximate thermal velocity dispersion for N_2H^+ at 15 K ($=0.066 \text{ km s}^{-1}$), and the sound speed for a mean molecular mass of 2.33 a.m.u ($=0.23 \text{ km s}^{-1}$), respectively. Vertical dashed lines refer to the location of H6 ($\Delta\delta = 21.71''$, $\Delta\alpha = 2.99''$), from BT12.

structures along the line of sight. Moreover, these filaments overlap towards the position of the most massive core in the region, H6 (Papers IV & V). Large-scale kinematic studies revealed the presence of three filaments, filament 1, $(42.95 \pm 0.17) \text{ km s}^{-1}$; filament 2 (the main IRDC filament), $(45.63 \pm 0.03) \text{ km s}^{-1}$; and filament 3, $(46.77 \pm 0.06) \text{ km s}^{-1}$ (Paper IV). Due to the high-angular resolution of this study, it is evident that filament 2 can be resolved into two separate structures, F2a ($45.34 \pm 0.04 \text{ km s}^{-1}$) and F2b ($46.00 \pm 0.05 \text{ km s}^{-1}$). In addition, the high-angular resolution PdBI map reveals that individual filaments can be both spectrally, and spatially resolved (see Section 3.1).

Figure 15 highlights the “spine”, i.e. the peak intensity for each filamentary structure identified in the PdBI data (as derived from the fitting routine outlined in Appendix D). This image has been generated by calculating an intensity-weighted offset right-ascension for every offset declination. The decomposition of G035.39-00.33 into multiple velocity components bears striking resemblance to the intricate filamentary structure observed in the L1495/B213 complex in Taurus identified by Hacar et al. (2013). In L1495/B213, a total of 35 structures have been identified. In addition, these filaments can be grouped into several “bundles” based on their chemical and kinematic properties. Hacar et al. (2013) suggest a possible hierarchical route of fragmentation from cloud \rightarrow bundles \rightarrow filaments \rightarrow cores. In the case of

G035.39-00.33, given the discussion posed in Section 5.1, it is interesting to ask the question, ‘*are the observed filaments part of the initial conditions of star formation, or are they a consequence of projection effects, and/or protostellar feedback?*’

Previous single-dish studies, papers IV and V, noted the presence of a large-scale ($\sim 2\text{--}3 \text{ pc}$) velocity gradient, with Paper V suggesting several plausible reasons for its origin. One scenario involves global accretion of material onto H6, along filament 2. In this scenario, estimating a mass accretion rate gives a value of the order $5 \times 10^{-3} M_{\odot} \text{ yr}^{-1}$, two orders of magnitude greater than the mass accretion rate estimated towards cluster forming regions in the Serpens molecular cloud (Kirk et al. 2013, Friesen et al. 2013). This may suggest that F2a and F2b actually represent a change in velocity (i.e. from low-to-high velocity), but are in fact still part of the same parent structure (filament 2). This “jump” in velocity would be similar to the velocity structure of collapsing filaments generated in numerical simulations of colliding flows by Gomez & Vazquez-Semadeni (2013). However, in order to simultaneously observe two spectral velocity components (as opposed to a single component that exhibits an abrupt change in velocity at the location of star formation; Gomez & Vazquez-Semadeni 2013) over a large spatial extent (as is observed in G035.39-00.33; see Figure 15), the filament would have to be aligned close to the line of sight. Whilst

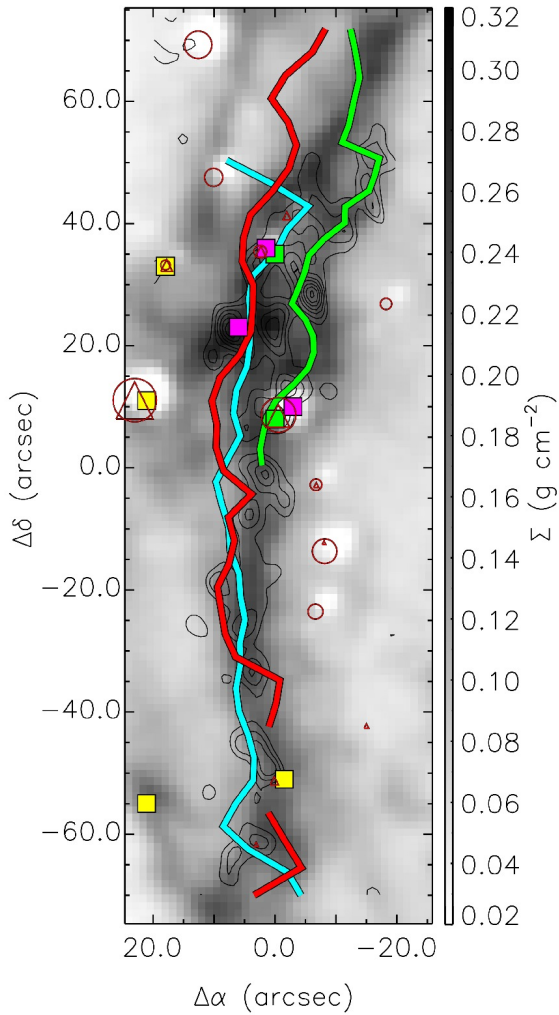


Figure 15. The peak intensity “spine” of each filament in G035.39-00.33, overlaid on the mass surface density map of KT13, and the 3.2 mm continuum contours. Cyan, red, and green refer to filaments F2a, F2b, and F3, respectively. The additional symbols, and contour values are identical to those in Figure 9.

this cannot be ruled out, G035.39-00.33 is extended over several parsecs in the plane of the sky, and therefore this seems unlikely.

An alternative scenario would be that F2a and F2b may represent the *radial* collapse of the filaments. This would explain why two spectral features are observed over a large spatial extent. In this scenario, F2a and F2b would represent the front and back of an inclined, radially collapsing filament. By inference therefore, this would mean that the N_2H^+ is depleted at intermediate velocities (as the optical depth of the isolated components is typically $\tau < 1$, as seen in Section 3.2). Although depletion of N_2H^+ has been observed towards low-mass starless cores (e.g. Bergin et al. 2002, Caselli et al. 2002b), the observed abundance decrease is typically only limited to a factor of ~ 2 . In addition, it is clear from Figure 4 that the observed integrated N_2H^+ emission rises with increasing mass surface density, suggestive of optically thin conditions and negligible depletion.

The PdBI data therefore imply that the global North-South

velocity gradient observed in single-dish data may, in fact, be explained by the presence of substructure within “filament 2” (i.e. F2a and F2b), and that this gradient does not transcend to smaller scales. The PdBI data indicates that the gas motions are dominated by *local* velocity gradients of the order $\sim 1.5\text{--}2.5 \text{ km s}^{-1} \text{ pc}^{-1}$, whereas global velocity gradients, and those observed in the North-South direction are smaller by comparison ($\sim 0.7 \text{ km s}^{-1} \text{ pc}^{-1}$, and $< 0.3 \text{ km s}^{-1} \text{ pc}^{-1}$, respectively; see Section 4.2). Given that the filaments are resolved spectrally, have differing velocity patterns, and (in the case of F2a/F2b and F3) are resolved spatially (c.f. Figure 3), we identify them as independent structures.

Away from H6, in the very South of F2a ($\Delta\delta < -50''$) and in the North of F2b ($\Delta\delta > 40''$), uniform gradients in the East \rightarrow West direction are observed. In addition, the velocity pattern observed in F2a at offset ($8'', -30''$) indicates that velocity increases towards the centre of the filament (see also Figure 1). This interesting feature is spatially coincident with a localised increase in the velocity dispersion (see Figure 10). Gradients such as these do not seem to be associated with any specific continuum peak. Thus, it is possible that these gradients may represent global motion of the filaments, rather than those related to the early stages of star formation (This is explored further in Appendix C, using position-velocity analysis).

The velocity dispersions observed in this study are *mildly* supersonic. The mean velocity dispersion (as calculated from the Gaussian fitting routine) across all three filaments is $\sim 0.33 \text{ km s}^{-1}$. Whilst the derived supersonic line-widths are in contrast to low-mass star forming filaments (e.g. Hacar et al. 2013, who find $\sigma_{\text{NT}}/c_s \sim 0.61 \pm 0.17$ using N_2H^+ towards the L1495/B213), they are narrower than those observed towards other IRDCs. Sanhueza et al. (2012) find that broad N_2H^+ line-widths are correlated with the star formation activity of clumps. They find line-widths in the range $1.6\text{--}4.6 \text{ km s}^{-1}$ (corresponding to dispersions of $\sim 0.7\text{--}2.0 \text{ km s}^{-1}$). Higher-spectral resolution studies are needed to verify results such as these in regions where a broad velocity dispersion may be explained by presence of unresolved spectral features. In regions where multiple spectral features are evident, moment analysis misleadingly indicates a larger dispersion than that of the individual components (by a factor of ~ 2 ; see Figure 1, and the spectrum at offset = $-4.24'', 10.77''$ in Figure 5, for example). Gaussian decomposition of the spectra is therefore a *necessity* in establishing the velocity dispersion of *individual* filaments.

The left hand panels of Figure 16 show how the non-thermal velocity dispersion of each individual filament changes with respect to the main beam brightness temperature at all positions in the cloud. In Paper III, the total velocity dispersion derived from the $\text{C}^{18}\text{O} (2-1)$ was identified to decrease towards the central, and dense portion of G035.39-00.33. Similarly, in Paper V, the relationship between the non-thermal dispersion and T_{MB} was studied for CO isotopologues, $^{13}\text{CO} (2-1)$, $^{13}\text{CO} (3-2)$, and $\text{C}^{18}\text{O} (2-1)$. In all cases σ_{NT} was shown to increase with decreasing T_{MB} with a power law trend. The dependency of σ_{NT} on T_{MB} was also shown to decrease with increasingly dense molecular tracers. In Figure 16, a similar trend for filaments F2a and F2b is found, in that there is an overall decrease of the non-thermal component with increasing brightness. In Pineda et al. (2010), studying star formation in the B5 region of Perseus, intensity (in this case antenna temperature) is used as a proxy for density. The trend of decreasing turbulent motion with increasing intensity therefore represents a “transition to coherence” within close proximity to the location of star forming cores.

In contrast to filaments F2a and F2b however, turbulent motion actually increases towards H6 in filament F3. This is evident

in the central, and right-hand panels of Figure 16. Here, the relationship between σ_{NT} , offset declination (central panels), and offset right ascension (right-hand panels) is plotted for each filamentary structure in G035.39-00.33. In the central and right-hand panels of F3, it is evident that the broadest lines, and therefore the lines with the greatest non-thermal component, are spatially coincident with H6. In low-mass star-forming regions, pre-stellar cores show slight ($\sim 60\%$) line broadening towards their centres, due to the infall of material (Crapsi et al. 2005). In G035.39-00.33, this peak is not directly coincident with the SW continuum core discussed in Section 5.1. Instead, the peak in the non-thermal velocity dispersion is coincident with a starless core to the North of here (see Figure 10). Higher-angular resolution observations of higher-density tracers are needed in order to understand the behaviour of star forming *cores* in relation to the surrounding dense filamentary material.

6 CONCLUSIONS

We have presented a detailed kinematic study using high-sensitivity and high-spectral resolution PdBI observations of N_2H^+ (1-0) towards a highly-filamentary IRDC. Our results and analysis lead us to conclude the following:

(i) Multiple filaments are identified both spectrally and spatially. F2a, F2b, and F3 have mean centroid velocities of $(45.34 \pm 0.04) \text{ km s}^{-1}$, $(46.00 \pm 0.05) \text{ km s}^{-1}$, $(46.86 \pm 0.04) \text{ km s}^{-1}$, respectively.

(ii) The abrupt change in velocity noted at the location of H6 (Papers IV & V), rather than being indicative of large scale flows towards H6, may be explained by the presence of substructure within filament 2, i.e. F2a and F2b.

(iii) F2a, F2b, and F3 have mean line-widths (FWHM) of $(0.83 \pm 0.04) \text{ km s}^{-1}$, $(0.77 \pm 0.04) \text{ km s}^{-1}$, and $(0.71 \pm 0.04) \text{ km s}^{-1}$, respectively. The ratio of non-thermal to thermal (for N_2H^+) velocity dispersion for each velocity component is 5.4, 5.0, and 4.7, respectively. The ratio of the non-thermal component of the line-width to the isothermal sound speed for an average molecule (mass = 2.33 a.m.u.) at 15 K are 1.6, 1.4, and 1.4, respectively. This indicates that the gas motions are *mildly* supersonic. In regions where multiple spectral components are evident, moment analysis can overestimate the non-thermal contribution to the line-width by a factor $\gtrsim 2$.

(iv) Globally, the kinematics of the gas are relatively quiescent, indicated by the small velocity gradients observed over each filament (of the order $< 0.7 \text{ km s}^{-1} \text{ pc}^{-1}$). Locally, however, the mean velocity gradients can reach $\sim 1.5\text{--}2.5 \text{ km s}^{-1} \text{ pc}^{-1}$.

(v) There is some indication that the kinematics of the dense gas may be influenced by the self-gravity of dense cores within filaments, or possibly by outflow feedback from already forming stars. Further molecular line observations are required to discern between these two scenarios. For these two opposing scenarios we calculate:

- (a) *Infall*: The mass accretion rate is estimated to be $\sim (7 \pm 4) \times 10^{-5} M_{\odot} \text{ yr}^{-1}$. The filaments retain their structure within the vicinity of H6, and individual filaments appear to feed individual cores. The SW continuum core could accrete an additional $(36 \pm 25) M_{\odot}$, in an estimated free-fall time of $(5 \pm 3) \times 10^5 \text{ yrs}$.
- (b) *Expanding shell*: The momentum for the expanding shell

is estimated to be $\sim (24 \pm 12) M_{\odot} \text{ km s}^{-1}$. The dense filamentary structures may have been separated from the main body of IRDC material due to the dynamic processes of star formation.

Our analysis highlights the importance of combining high-sensitivity and high-spectral resolution data at high-angular resolution, to put quantitative constraints on the dynamics of high-mass star forming regions.

7 ACKNOWLEDGMENTS

We thank the anonymous referee for his/her careful reading of the manuscript, and for their detailed comments that have helped to improve the clarity of the paper. J. Henshaw would like to thank Alvaro Hacar, Andy Pon, and Dinshaw Balsara for the useful discussions on filaments. In addition, we would like to thank Michael Butler, and Jouni Kainulainen for providing us with the mass surface density maps. We would like to thank the IRAM staff for their help throughout the reduction and CLEANing process. J. Henshaw gratefully acknowledges support provided by the Science and Technologies Faculties Council (STFC). P. Caselli acknowledges the financial support of the European Research Council (ERC; project PALs 320620) and of successive rolling grants awarded by the UK Science and Technology Funding Council. I. Jiménez-Serra acknowledges funding from the People Programme (Marie Curie Actions) of the European Union's Seventh Framework Programme (FP7/2007-2013) under REA grant agreement number PIFI-GA-2011-301538. J. C. Tan acknowledges support from NSF CAREER grant AST-0645412; NASA Astrophysics Theory and Fundamental Physics grant ATP09-0094; NASA Astrophysics Data Analysis Program ADAP10-0110. This work has benefited from research funding from the European Community's Seventh Framework Programme.

REFERENCES

- Arce H. G., Borkin M. A., Goodman A. A., Pineda J. E., Beaumont C. N., 2011, *ApJ*, 742, 105
- Balsara D., Ward-Thompson D., Crutcher R. M., 2001, *MNRAS*, 327, 715
- Bergin E. A., Alves J., Huard T., Lada C. J., 2002, *ApJL*, 570, L101
- Busquet G. et al., 2013, *ApJL*, 764, L26
- Butler M. J., Tan J. C., 2009, *ApJ*, 696, 484
- Butler M. J., Tan J. C., 2012, *ApJ*, 754, 5
- Carey S. J., Clark F. O., Egan M. P., Price S. D., Shipman R. F., Kuchar T. A., 1998, *ApJ*, 508, 721
- Carey S. J. et al., 2009, *PASP*, 121, 76
- Caselli P., Benson P. J., Myers P. C., Tafalla M., 2002a, *ApJ*, 572, 238
- Caselli P., Myers P. C., 1995, *ApJ*, 446, 665
- Caselli P., Myers P. C., Thaddeus P., 1995, *ApJL*, 455, L77+
- Caselli P., Walmsley C. M., Zucconi A., Tafalla M., Dore L., Myers P. C., 2002b, *ApJ*, 565, 344
- Chambers E. T., Jackson J. M., Rathborne J. M., Simon R., 2009, *ApJS*, 181, 360
- Chira R.-A., Beuther H., Linz H., Schuller F., Walmsley C. M., Menten K. M., Bronfman L., 2013, *A&A*, 552, A40
- Crapsi A. et al., 2005, *A&A*, 439, 1023
- Csengeri T., Bontemps S., Schneider N., Motte F., Gueth F., Hora J. L., 2011, *ApJL*, 740, L5

Daniel F., Dubernet M.-L., Meuwly M., Cernicharo J., Pagani L., 2005, *MNRAS*, 363, 1083

Devine K. E., Chandler C. J., Brogan C., Churchwell E., Indebetouw R., Shirley Y., Borg K. J., 2011, *ApJ*, 733, 44

Egan M. P., Shipman R. F., Price S. D., Carey S. J., Clark F. O., Cohen M., 1998, *ApJL*, 494, L199+

Fiege J. D., Pudritz R. E., 2000, *MNRAS*, 311, 85

Fontani F., Caselli P., Bourke T. L., Cesaroni R., Brand J., 2008, *A&A*, 477, L45

Fontani F., Giannetti A., Beltrán M. T., Dodson R., Rioja M., Brand J., Caselli P., Cesaroni R., 2012, *MNRAS*, 423, 2342

Friesen R. K., Medeiros L., Schnee S., Bourke T. L., Francesco J. D., Gutermuth R., Myers P. C., 2013, *MNRAS*, 436, 1513

Fuller G. A., Myers P. C., 1992, *ApJ*, 384, 523

Gomez G. C., Vazquez-Semadeni E., 2013, *ArXiv e-prints*, arXiv:1308.6298

Goodman A. A., Benson P. J., Fuller G. A., Myers P. C., 1993, *ApJ*, 406, 528

Hacar A., Tafalla M., Kauffmann J., Kovács A., 2013, *A&A*, 554, A55

Henshaw J. D., Caselli P., Fontani F., Jiménez-Serra I., Tan J. C., Hernandez A. K., 2013, *MNRAS*, 428, 3425, (Paper IV)

Hernandez A. K., Tan J. C., Caselli P., Butler M. J., Jiménez-Serra I., Fontani F., Barnes P., 2011, *ApJ*, 738, 11, (Paper II)

Hernandez A. K., Tan J. C., Kainulainen J., Caselli P., Butler M. J., Jiménez-Serra I., Fontani F., 2012, *ApJL*, 756, L13, (Paper III)

Hily-Blant P., Teyssier D., Philipp S., Güsten R., 2005, *A&A*, 440, 909

Jimenez-Serra I., Caselli P., Fontani F., Tan J. C., Henshaw J. D., Kainulainen J., Hernandez A. K., 2014, *ArXiv e-prints*, arXiv:1401.2347 (Paper V)

Jiménez-Serra I., Caselli P., Tan J. C., Hernandez A. K., Fontani F., Butler M. J., van Loo S., 2010, *MNRAS*, 406, 187, (Paper I)

Kainulainen J., Tan J. C., 2013, *A&A*, 549, A53

Kirk H., Myers P. C., Bourke T. L., Gutermuth R. A., Hedden A., Wilson G. W., 2013, *ApJ*, 766, 115

Markwardt C. B., 2009, in *Astronomical Society of the Pacific Conference Series*, Vol. 411, *Astronomical Data Analysis Software and Systems XVIII*, Bohlender D. A., Durand D., Dowler P., eds., p. 251

Myers P. C., 1983, *ApJ*, 270, 105

Myers P. C., 2005, *ApJ*, 623, 280

Nguyen Luong Q. et al., 2011, *A&A*, 535, A76

Ostriker J., 1964, *ApJ*, 140, 1056

Pagani L., Daniel F., Dubernet M., 2009, *A&A*, 494, 719

Pérault M. et al., 1996, *A&A*, 315, L165

Peretto N. et al., 2014, *A&A*, 561, A83

Peretto N. et al., 2013, *A&A*, 555, A112

Peretto N. et al., 2010, *A&A*, 518, L98

Peretto N., Hennebelle P., André P., 2007, *A&A*, 464, 983

Pillai T., Wyrowski F., Carey S. J., Menten K. M., 2006, *A&A*, 450, 569

Pineda J. E., Goodman A. A., Arce H. G., Caselli P., Foster J. B., Myers P. C., Rosolowsky E. W., 2010, *ApJL*, 712, L116

Pon A., Johnstone D., Heitsch F., 2011, *ApJ*, 740, 88

Pon A., Toalá J. A., Johnstone D., Vázquez-Semadeni E., Heitsch F., Gómez G. C., 2012, *ApJ*, 756, 145

Quillen A. C., Thorndike S. L., Cunningham A., Frank A., Gutermuth R. A., Blackman E. G., Pipher J. L., Ridge N., 2005, *ApJ*, 632, 941

Ragan S. E., Bergin E. A., Wilner D., 2011, *ApJ*, 736, 163

Rathborne J. M., Jackson J. M., Simon R., 2006, *ApJ*, 641, 389

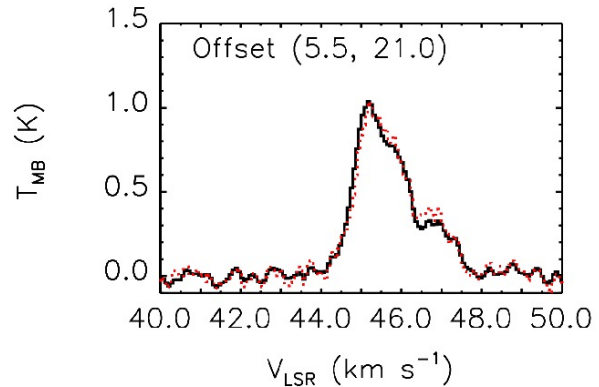


Figure A1. Comparison between the merged PdBI and IRAM 30 m N_2H^+ ($1 - 0$) data (black solid line; smoothed equivalent resolution of the single-dish data), and the IRAM 30 m data only (red dotted line), at the location of H6 (only the isolated hyperfine component is shown).

Sanhueza P., Jackson J. M., Foster J. B., Garay G., Silva A., Finn S. C., 2012, *ApJ*, 756, 60

Sanhueza P., Jackson J. M., Foster J. B., Jimenez-Serra I., Dirienzo W. J., Pillai T., 2013, *ApJ*, 773, 123

Schneider N., Csengeri T., Bontemps S., Motte F., Simon R., Hennebelle P., Federrath C., Klessen R., 2010, *A&A*, 520, A49

Schöier F. L., van der Tak F. F. S., van Dishoeck E. F., Black J. H., 2005, *A&A*, 432, 369

Simon R., Rathborne J. M., Shah R. Y., Jackson J. M., Chambers E. T., 2006, *ApJ*, 653, 1325

Stodólkiewicz J. S., 1963, *Acta Astronomica*, 13, 30

Tan J. C., Shaske S. N., Van Loo S., 2013, in *IAU Symposium*, Vol. 292, *IAU Symposium*, Wong T., Ott J., eds., pp. 19–28

Tobin J. J. et al., 2013, *ApJ*, 765, 18

APPENDIX A: EXAMPLE SPECTRA

Figure A1 shows spectra of the merged PdBI and IRAM 30 m N_2H^+ ($1 - 0$) data (only the isolated component has been shown), smoothed to the equivalent resolution of the 30 m map, close to H6 (black solid line). This has been compared with the IRAM 30 m only data (red dotted line). This indicates that combined data cannot suffer from missing flux.

Figure A2 shows the full spectrum (including all hyperfine components) at offset = (3.6'', 12.7''). The hyperfine structure of the N_2H^+ ($1 - 0$) line can be used to estimate the optical depth of the individual velocity components. Overlaid are markers indicating the velocities of hyperfine components corresponding to F2a (cyan), F2b (red), and F3 (green), using the parameters extracted from the fitting procedure outlined in Appendix D. The height of each line corresponds to the expected intensity of individual hyperfine components assuming optically thin conditions. The solid curve represents a 3 component hyperfine structure fit performed using the GILDAS/CLASS software. The *total* optical depth of the fitted lines are 5.28 (0.12), 7.92 (0.10), 0.11 (0.05), respectively. For the isolated hyperfine components therefore these values give optical depths of 0.7, 0.9, 0.01. This indicates that the isolated components are *partially* optically thick towards the H6 region. However, given the relatively small optical depth values, the corresponding correction factors would also be small. Whilst the hyperfine struc-

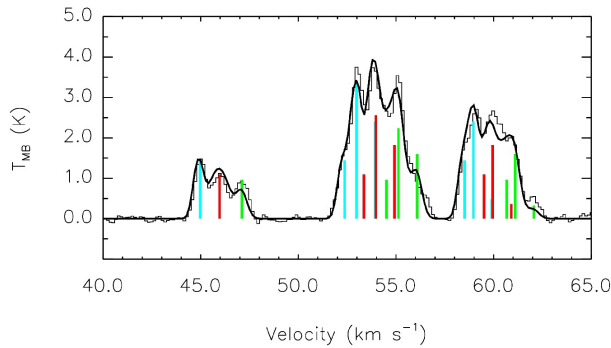


Figure A2. N_2H^+ (1 – 0) spectrum from offset = (3.6'', 12.7''). Coloured lines indicate respective velocities of all hyperfine components of individual velocity components (F2a is plotted in cyan, F2b in red, and F3 in green). The velocities and intensities of the isolated hyperfine components are derived using the fitting procedure outlined in Appendix D. The velocities of the remaining hyperfine components are then established from their velocity separation, and their intensities are estimated using the respective statistical weights (assuming LTE). The solid black line is the result of a hyperfine structure fit, incorporating the three velocity components observed.

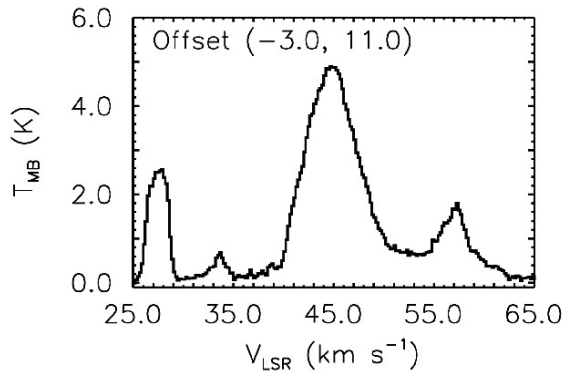


Figure A3. CO (1 – 0) IRAM 30 m data observed towards the SW core (see Section 5.1.2).

ture *can* be fitted in some locations, fitting routines may converge to ambiguous results. This is due to the blending of spectral components.

Figure A3 shows the CO (1 – 0) spectrum at the location of the SW core (see Section 5.1.2), centred on offset (-3.0'', 11.0''). The spatial resolution is 21.5'', and the spectral resolution is 0.2 km s⁻¹.

APPENDIX B: FIT PARAMETERS

See Table B1.

APPENDIX C: POSITION-VELOCITY ANALYSIS

Figure C1 shows the dissection of G035.39-00.33 into slices that have been selected for PV analysis. Two major longitudinal cuts (A and B, shown in dot-dashed red and solid cyan, respectively, with A

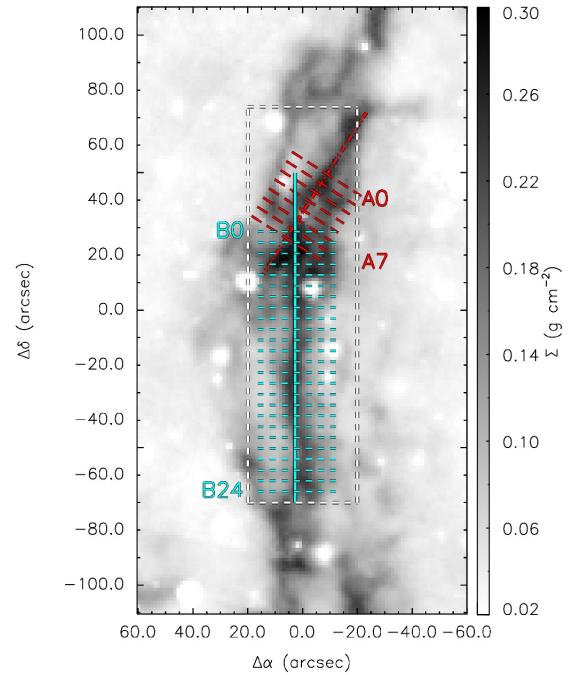


Figure C1. Mass surface density plot from KT13, overlaid with locations of the PV slices discussed in Section C. Dot-dashed red and solid cyan lines indicate the longitudinal cuts taken from North to South, and dashed lines represent radial slices. Radial slices have been numbered from A0–A7 in the case of cut A and B0–B24 in the case of cut B. The dashed white box shows the extent of the PdBI map in N_2H^+ (1 – 0).

being the most northerly) have been selected based on the densest regions of the cloud (as seen in *extinction*). In this Appendix the gas motions both along the main axis of the IRDC, and perpendicular to it are explored.

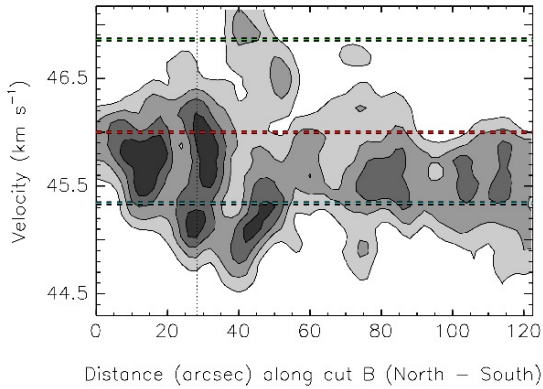
The lower limit of Σ that can be probed is $\sim 0.007 \text{ g cm}^{-2}$ (which corresponds to an extinction, $A_v = 1.6 \text{ mag}$; this is for the NIR map only, see KT13 for discussion). For the gas motions along the main axis slices are defined by only considering mass surface density values with $\Sigma \geq 9 \times$ this lower limit, i.e. 0.063 g cm^{-2} (corresponding to $A_v = 14.5 \text{ mag}$). This ensures that only the brightest N_2H^+ emission is focused on (Figures 1 and 4 show the close relationship between mass surface density and N_2H^+ emission). For the slice definition, an intensity-weighted mean offset right ascension was calculated at each increment in offset declination. The mean of these values was then used to make the longitudinal cuts (red dot-dashed and solid cyan lines in Figure C1).

Figures 14 & C2 show PV cuts A & B (identified by dot-dashed red and solid cyan lines in Figure C1). Figures C3 & C4 show the PV data perpendicular to the slices A and B (from East–West), as highlighted in Figure C1 (dashed lines). 8 and 25 slices are taken perpendicular to cut A and cut B, respectively. Each slice is separated by 2 pixels. In all Figures, black contours show the 5σ , 10σ , 15σ , and 20σ levels ($\sigma = \text{mean rms} = 0.1 \text{ K}$).

Velocity gradients are evident throughout G035.39-00.33. The emission along slices A & B suggest overall negative velocity gradients from North to South. In the case of cut A, this “gradient” may in fact be due to the emergence of additional components. Filaments F2a and F2b exist at distances $> 40''$ along the slice, whereas F3 is mainly present North of this location (see Section 4 for more

Table B1. Fit parameters for the Gaussian fits to the spectra shown in Figure 5.

Filament	$\Delta\alpha$ ($''$)	$\Delta\delta$ ($''$)	T_{peak} (K)	σT_{peak} (K)	V_{LSR} (km s^{-1})	σV_{LSR} (km s^{-1})	Δv (km s^{-1})	$\sigma \Delta v$ (km s^{-1})	RMS (K)	Residual (std dev) (K)
F2b	-16.06	69.87	1.38	0.17	46.12	0.08	0.72	0.04	0.09	0.09
F3	-16.06	69.87	0.86	0.21	46.75	0.11	0.67	0.06	0.09	0.09
F2a	3.64	22.59	1.92	0.04	45.20	0.01	0.63	0.01	0.04	0.03
F2b	3.64	22.59	2.09	0.02	46.06	0.01	0.91	0.01	0.04	0.03
F2a	-4.24	10.77	0.76	0.03	45.05	0.02	0.87	0.02	0.06	0.08
F3	-4.24	10.77	0.77	0.03	47.29	0.02	1.03	0.02	0.06	0.08
F2a	7.58	8.80	0.70	0.07	44.82	0.05	0.69	0.04	0.08	0.10
F2b	7.58	8.80	1.43	0.05	45.93	0.03	1.12	0.05	0.08	0.10
F3	7.58	8.80	0.60	0.07	47.03	0.04	0.62	0.04	0.08	0.10

**Figure C2.** Position-Velocity diagram of cut B (see cyan solid line in Figure C1). The filled contours are in units of main beam brightness temperature and correspond to the 5σ , 10σ , 15σ , and 20σ levels (where $\sigma = \text{mean RMS} = 0.1 \text{ K}$). The vertical dotted line represents the position of H6 along the length of the PV slice. Horizontal dashed lines refer to the mean V_{LSR} of each of the three filaments F2a, F2b, and F3 (seen in cyan, red, and green, respectively).

details on the location of filaments). In cut B however, both F2a and F2b are present over the full length, and so any change in velocity with respect to distance along the PV slice, may indeed be representative of a velocity gradient.

Multiple velocity components are present throughout the PV slices. In cut B (Figure C2) it is evident that the broadest velocity span is present between $40'' \lesssim \text{distance along cut B} \lesssim 50''$ (with corresponding offsets: $0'' \lesssim \Delta\delta \lesssim 10''$), confirming the result seen in Figure 8. Multiple velocity components are also observed in the radial PV slices (Figures C3 & C4). The frequency at which these components are observed increases closer to H6. In Figure C3 (slice A6) filaments F2a, F2b, and F3 are identified in the diagram, exhibiting separations in both position and velocity.

There is a common elongation in the emission between the peaks identified as filaments F2a and F2b in a number of PV slices. Whilst this is also evident close to H6 (see for example slices A5, A6, A7, B1, B2, B5), it is preferable to estimate the magnitude of this gradient away from the complexity of this location. Between $-40'' < \Delta\delta < -15''$, i.e. South of H6, there is a peak in N_2H^+ emission that is IR-quiet (c.f. Figure 1, Carey et al. 2009, Paper V). This emission is covered in Figure C4 by slices B12–B16. The magnitude of this gradient is estimated by firstly selecting the emission $> 9\sigma$, in the black dashed boxes shown in Figure C4 (criteria (i)

Busquet et al. 2013: filament emission defined to have $\text{SNR} > 9$), and secondly, selecting PV slices within which the 9σ emission extends over at least $2 \times$ the map resolution ($10.6''$). An intensity weighted position for each incremental step in velocity contained within the selected area is then calculated. Following similar analysis to Hily-Blant et al. (2005), who investigated rotation in the Horsehead nebula, a linear fit is calculated (under the assumption of solid body rotation) for each box using the intensity weighted position versus velocity. The mean magnitude of this gradient is $(-13.9 \pm 2.0) \text{ km s}^{-1} \text{ pc}^{-1}$. In the analysis of Hily-Blant et al. (2005), the authors favour an interpretation of rotation rather than shear motion whilst studying the Horsehead nebula. In the case of G035.39-00.33, this may be indicative of shear motions between filaments. Such shear motions have been discussed in relation to the formation of massive dense cores in DR21 (OH) by Csengeri et al. (2011), who report velocity shears of $2\text{--}3 \text{ km s}^{-1}$. However, due to the relatively small angular separation of the two filaments, and considering the uncertainties that arise due to projection effects, this result is approached with caution.

APPENDIX D: GAUSSIAN FITTING & FILAMENT CLASSIFICATION

In this paper a semi-automated fitting routine has been used to identify multiple Gaussian components with spectra. The routine consists of two main components: A Gaussian fitting procedure, and a classification routine that identifies and groups components. In the next two sections the step-by-step methodology from fitting to classification is described.

D1 Fitting routine

(i) Firstly, a coverage is defined. The user is asked to provide a radius and spacing. This refers to a radius of a circle, within which the routine will compute an average spectrum from all spectra contained within this limit. The spacing refers to the placement of these preliminary areas. Specifically, it is an integer number of pixels, starting at the first position in the map. The radius and spacing number should be selected such that a complete coverage of the map is achieved. The radius should be large enough to sufficiently reduce user input, but small enough to avoid diluting the main features within the spectra. For this particular data set, a radius of $6''$, with a spacing of $5.91''$ (i.e. $1.5 \times$ pixels), was used. This provided full coverage with 175 preliminary areas.

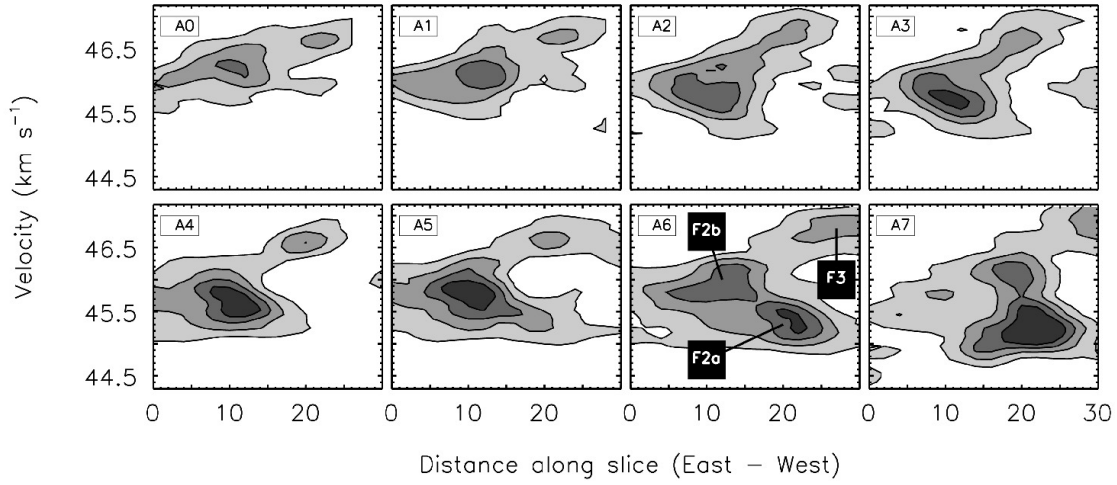


Figure C3. Position-Velocity diagrams of the 8 slices perpendicular to cut A indicated by dashed red lines in Figure C1. The filled contours are in units of main beam brightness temperature, and correspond to the 5σ , 10σ , 15σ , and 20σ levels (where $\sigma = \text{mean rms} \sim 0.1 \text{ K}$). The three filaments F2a, F2b, and F3, are clearly seen as emission peaks in slice A6.

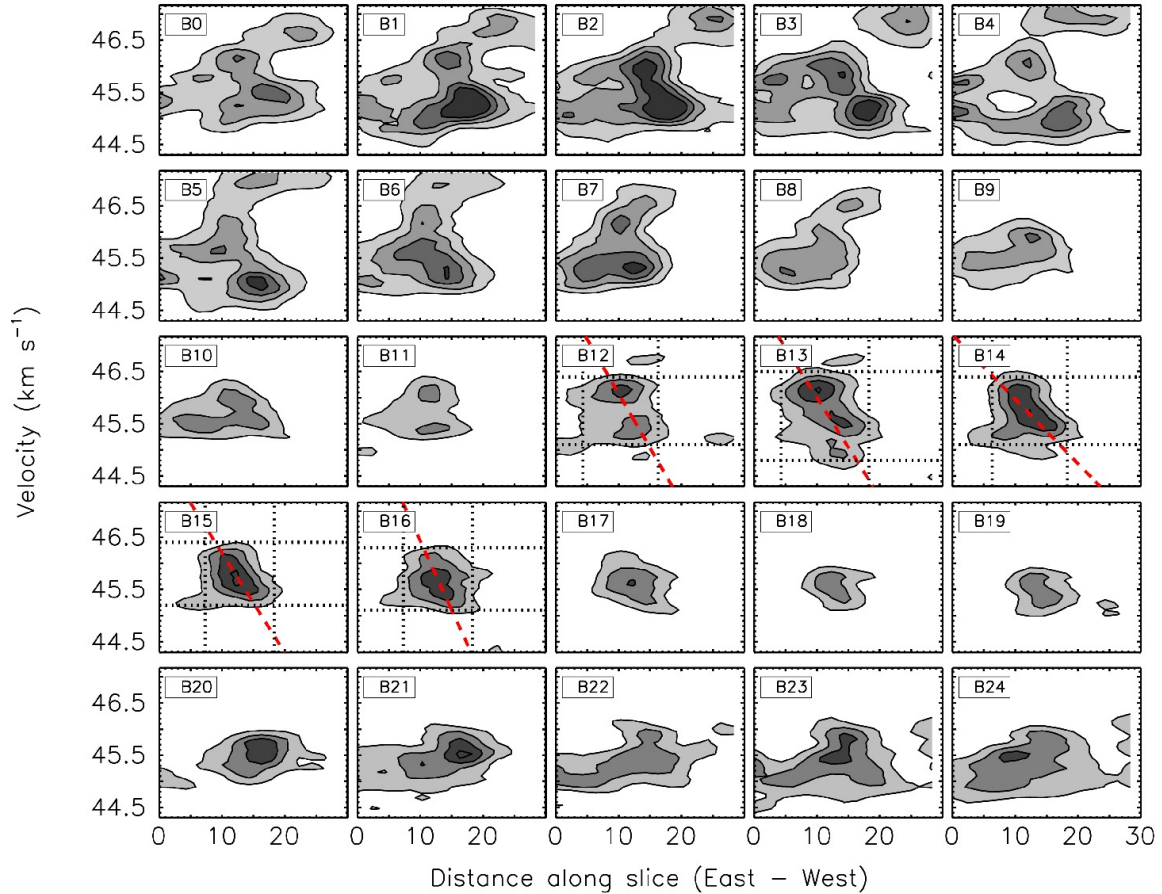


Figure C4. Same as Figure C3 but for the 25 slices perpendicular to cut B, see dashed cyan lines in Figure C1. The black dotted lines in boxes B12–B16 represent the limits over which the velocity gradient (red dashed line) has been calculated. For more information, see Section C.

(ii) For each area, all spectra contained within the confining radius are averaged. The user then defines how many Gaussian components to fit to each average spectrum, and to provide initial estimates for the intensity, velocity, and line-width of each component.

(iii) A minimisation algorithm, MPFITFUN (Markwardt 2009), is used to find best fit results for the single or multiple Gaussian components, displaying the result to the screen. The MPFITFUN fit results are then used as initial (free-parameter) estimates for each individual spectrum contained within the preliminary area.

(iv) The cycle is complete when no more preliminary areas remain.

The fitting routine allows the user to fit up to three Gaussian components at a time. In doing so, the routine outputs the following parameters for each individual Gaussian component: Ra, Dec, line intensity (with uncertainty), centroid velocity (with uncertainty), FWHM (with uncertainty), base RMS, χ_{red}^2 , residual value. The base RMS is calculated within a user defined velocity range. The χ_{red}^2 and residual values are derived from the output parameters of MPFITFUN. In order for the routine to identify multiple velocity components, it must satisfy a number of constraints:

(i) The spectrum must contain a velocity channel with a measured intensity greater than a user defined intensity threshold (based on the RMS). All positions that do not contain a velocity channel with intensity greater than this threshold are discarded.

(ii) The FWHM of all Gaussian components must be broader than the velocity resolution (Δv_{res}). Although simplistic, in very rare occasions the minimisation algorithm can converge on a non-physical solution - typically an extremely narrow (FWHM $\ll \Delta v_{\text{res}}$), and bright velocity component. These solutions are discarded by the program, and the spectra refit.

(iii) The separation in centroid velocity between two peaks must be greater than the half-width at half-maximum (HWHM) of the brightest component defined by the average spectrum. This is to prevent the minimisation algorithm converging towards a two component fit, when the spectrum only shows a single peak.

(iv) The centroid velocity of each Gaussian component in individual spectra must lie within a velocity range defined by $V_{\text{LSR}} - \text{FWHM}_{\text{av}} < V_{\text{LSR}} < V_{\text{LSR}} + \text{FWHM}_{\text{av}}$, where FWHM_{av} refers to the FWHM of the *same component* identified in the average spectrum. This ensures that the same velocity component is fitted in each spectrum, whilst also allowing for velocity gradients on a spectrum-to-spectrum basis.

If the above conditions are not satisfied, the program will aim to fit a lower amount of velocity components, repeating the above checks until they are satisfied. Once satisfied, in order to be verified as a fit, the residual value of the resultant fit must be less than 3σ .

Due to the preliminary areas having some level of overlap with neighbouring areas, there are typically multiple fits to the same position. In order to select the “best fit” to the spectrum, the fit with the lowest χ_{red}^2 is therefore chosen.

D2 Classification routine

To group velocity components, the map is divided into boxes. Each box has an area of $\sim 12'' \times 12''$ (the equivalent area would contain 9 synthesised PdBI beams). Next, the box with the greatest total integrated intensity is identified. Velocity component classification begins within this box using the following procedure:

(i) From the data-set containing the Gaussian fits, the position within the box with the greatest integrated intensity is selected: this

is the “seed” position. It is identified whether or not this position has multiple velocity components associated with it. The first velocity component is selected.

(ii) The angular distance to every position within the area is calculated using:

$$d_i = \sqrt{(X_{\text{seed/branch}} - X_i)^2 + (Y_{\text{seed/branch}} - Y_i)^2} \quad (\text{D1})$$

(see step (iv) for “branch” explanation).

(iii) All positions within a radius equivalent to the maximum distance between two adjacent points in the grid are selected. For the PdBI map this is equivalent to $\sqrt{(1.94)^2 + (1.94)^2} \sim 2.75''$ or ~ 0.04 pc at a distance of 2900 pc.

(iv) Each of these positions is then cycled through, calculating the velocity gradient between each spectral component, and the velocity component of the seed position ($\nabla v \equiv \frac{|V_i - V_{\text{seed/branch}}|}{d_i}$, where V_i is the velocity component of the selected position, $V_{\text{seed/branch}}$ is the velocity component of the seed (branch) position, and d_i is the angular distance defined in step (ii)). If the velocity gradient is $\leq 2 \text{ km s}^{-1} \text{ pc}^{-1}$ (which corresponds to a velocity difference of 0.08 km s^{-1} over a distance of 0.04 pc) then accept these components as linked. If linked, this position is registered as a new “branch” location.

(v) Fit components that have then been classified as linked, are then removed from the data set. This ensures no component will be linked twice.

(vi) Each *branch* location is now cycled through, repeating steps (ii)–(v). However, rather than using the seed velocity, the branch velocity is used.

(vii) Once no more branch locations can be attributed to the original seed, the next seed velocity component is selected and steps (ii)–(v) are repeated.

(viii) This continues until all velocity components from the seed have been exhausted.

(ix) Steps (i)–(viii) are repeated until all seed locations have then been exhausted.

This method groups Gaussian components that are *closely* linked in velocity (the initial linking gradient is \sim half of the velocity resolution in the case of the PdBI data). Therefore, this method leaves a number of points that do not meet the criteria outlined in step (iv) above. In order to group the unassigned data, angular distance from the brightest position in the cloud versus V_{LSR} is plotted for every Gaussian component within the area. Easily distinguished are the velocity components that have been fitted according to the method outlined above. The remaining unassigned data points were then linked to the group that is closest in velocity. If this presented an ambiguous result, for example in a box where two components converge into a single Gaussian fit, with no obvious asymmetry, then the data point remains unassigned. This analysis is repeated for each box in the mapped area.

At this point, all boxes are *independent* from the surrounding areas. In order to link velocity components between boxes, the brightest box is selected first, and the eight contiguous boxes are arranged in order of descending *total* integrated intensity. By linking boxes that are directly adjacent to one another the risk of linking different velocity components is minimised (maximum distance between two points in adjacent boxes $\sim 34''$; or ~ 0.5 pc at a distance of 2900 pc). Finally, once the procedure is complete, individual positions are checked by hand to see whether or not a different number of velocity components would better represent the data.

Table D1 highlights some statistics on the fitting procedure. Out of 1554 positions in the mapped region, a total of 1117 have

Table D1. Statistics regarding the fitting and classification procedures.

Attribute	value
Total number of pixels	1554
Total number of pixels fitted	1117
Percentage number of fits (%)	71.9
Number of positions refitted (%)	<10.0
Total number of Gaussians fitted	1700
Degree of multiplicity (components per pixel)	1.5
F2a (%)	40.5
F2b (%)	35.3
F3 (%)	15.6
C4 (%)	1.4
C5 (%)	<1.0
C6 (%)	<1.0
Unclassified data (%)	5.9

been fitted with a total of 1700 Gaussian components. This highlights the degree of multiplicity in the cloud and the complexity of the spectra. Following the above procedures, $\sim 9\%$ of the positions were refitted by hand. The majority of components have been attributed to filaments F2a, F2b, and F3, with contributions from additional components at various positions in the cloud (C4, C5, and C6 are identified as individual components, but cannot be linked to either each other or F2a, F2b, and F3, due to separation in either velocity or position). In total $\sim 6\%$ of the fits remain unclassified.